Journal of Power Sources 488 (2021) 229368

Contents lists available at ScienceDirect

Journal of Power Sources

journal homepage: www.elsevier.com/locate/jpowsour

Heat generation in electric double layer capacitors with neat and diluted ionic liquid electrolytes under large potential window between 5 and 80 °C

Ampol Likitchatchawankun [a], Ryan H. DeBlock [b], Grace Whang [b], Obaidallah Munteshari [a,c], Matevž Frajnkovič [a], Bruce S. Dunn [b,d], Laurent Pilon [a,d,e,*]

[a] Mechanical and Aerospace Engineering Department, Henry Samueli School of Engineering and Applied Science, University of California, Los Angeles, CA 90095, USA
[b] Materials Science and Engineering Department, Henry Samueli School of Engineering and Applied Science, University of California, Los Angeles, CA 90095, USA
[c] Mechanical Engineering Department, King Fahd University of Petroleum and Minerals (KFUPM), Dhahran 31261, Saudi Arabia
[d] California NanoSystems Institute, University of California, Los Angeles, Los Angeles, CA 90095, USA
[e] Institute of the Environment and Sustainability, University of California, Los Angeles, Los Angeles, CA 90095, USA

ARTICLE INFO

Keywords:
Activated carbon
Electrolyte degradation
Ionic liquid
Heat generation
Thermal management
Thermal runaway

ABSTRACT

This study investigates the effect of temperature on the heat generation and the associated electrochemical phenomena occurring in IL-based EDLCs. The EDLCs consisted of two identical activated carbon electrodes with neat $Pyr_{14}TFSI$ or $Pyr_{14}TFSI$ diluted in propylene carbonate (PC) as electrolytes. The instantaneous heat generation rate at each electrode was measured by isothermal calorimetry between 5 and 80 °C under constant current cycling and potential window of 2.5 V. First, the instantaneous heat generation rate was similar at each electrode in neat IL. However, it was smaller at the negative electrode in diluted IL and featured endothermic dips growing with increasing temperature >40 °C due to overscreening effects, ion desolvation, and/or decomposition of PC. The irreversible heat generation was similar in each half-cell and decreased with increasing temperature due to the reduction in internal resistance, particularly with neat IL. The irreversible heat generation exceeded Joule heating in all cases, especially at high temperature and low current. This was attributed to ion desorption and charge redistribution in the porous electrodes. Finally, the reversible heat generation for both electrolytes was larger at the positive than at the negative electrode due to the difference in anion and cation sizes.

1. Introduction

Electric double layer capacitors (EDLCs) feature large power densities, high cycle efficiency, and long cycle life [1–11]. They have received significant interest for applications requiring charging/discharging at high rates such as the utility grid and regenerative braking in hybrid or electric vehicles [1–11]. EDLCs consist typically of two carbon-based electrodes and a separator immersed in concentrated aqueous, organic, or ionic liquid-based electrolytes [12,13]. They store electrical energy in the electric double layer (EDL) formed by ions at the porous electrode/electrolyte interface [10–13]. Their energy density E (in J/m^2) can be expressed as [1],

$$E = \frac{1}{2} C \, \Delta\psi_s^2 \tag{1}$$

where C is the specific capacitance of the cell (in F/m^2) and $\Delta\psi_s$ is the potential window (in V). Increasing $\Delta\psi_s$ can significantly increase the energy density E. However, $\Delta\psi_s$ is limited by the electrochemical stability of the electrolyte [1]. Similarly, increasing temperature moderately enhances ion transport and increases the capacitance C. However, in high power applications, EDLCs can experience a considerable amount of heat generation resulting in excessively high cell temperature [8,9,14,15]. Elevated temperatures, in turn, can lead to (i) accelerated aging of the device [8,9,14–18], (ii) increased self-discharge rate [14,15,17], and (iii) thermal decomposition of the electrolyte [17–19].

Ionic liquids (ILs) and their mixtures have been considered as promising electrolytes for EDLCs for their good thermal stability [20–25], wide operating potential windows [23–28], and operation at low temperatures [21,24,28,29]. However, neat ILs typically suffer from low ionic conductivity (~ 1 to 20 mS/cm at room temperature) [20,22,30–34] compared with aqueous electrolytes (~ 200 to 800 mS/cm) [33,

* Corresponding author at: Mechanical and Aerospace Engineering Department, Henry Samueli School of Engineering and Applied Science, University of California, Los Angeles, CA 90095, USA.
E-mail address: pilon@seas.ucla.edu (L. Pilon).

https://doi.org/10.1016/j.jpowsour.2020.229368
Received 3 August 2020; Received in revised form 3 December 2020; Accepted 16 December 2020
0378-7753/

Nomenclature

A	Footprint area of the heat flux sensor, cm^2
$C_{diff,m}$	Gravimetric differential capacitance, F/g
$C_{int,m}$	Gravimetric integral capacitance, F/g
D	Diffusion coefficient, m^2/s
I	Current, mA
i	Current density, mA/cm^2
m	Mass loading of active material in electrode, mg
n_c	Cycle number, –
q''	Heat flux, mW/cm^2
$\dot{Q}$	Heat generation rate, mW
$\bar{\dot{Q}}$	Time-averaged heat generation rate, mW
R	Resistance, Ω
R_s	Internal resistance for entire device, Ω
S	Heat flux sensor sensitivity, $\mu V/(W/cm^2)$
t	Time, s
t_c^-	Time immediately after the beginning of the discharging step, s
t_c^+	Time at the end of the charging step, s
T	Temperature or absolute temperature, °C or K
ΔV	Voltage difference generated in the heat flux sensor, μV
z_i	Valency, –

Greek symbols

ϵ_r	Dielectric constant, –
ν	Scan rate, mV/s
σ	Ionic conductivity, mS/cm
$\psi_{s,min}, \psi_{s,max}$	Minimum, maximum cell potential, V
$\psi_s(t)$	Cell potential, V

Superscripts and subscripts

c	Refers to charging step
cd	Refers to charging–discharging cycle
d	Refers to discharging step
i	Refers to ion species "i"
J	Refers to Joule heating
T	Refers to entire cell
rev,i	Refers to reversible heat generation
+ or −	Refers to positive or negative electrode

34]. Nevertheless, their ionic conductivity increases strongly with increasing temperature [20,35–38]. Another way to increase the ionic conductivity of ILs is to dilute them in carbonate-based organic solvents such as propylene carbonate (PC) or a mixture of ethylene carbonate (EC)- dimethyl carbonate (DMC) as well as in nitrile-based solvent such as acetonitrile (ACN) [20,21,39]. The increase in ionic conductivity and the associated decrease in viscosity in diluted ILs are due to the reduction in ion pairing via solvation [21]. However, diluted ILs tend to be less electrochemically and thermally stable than their neat IL counterpart [21]. In addition, despite the wide theoretical potential window of ILs, they may react with the carbonaceous electrode surface as a result of catalytic activity [40,41]. Moreover, elevated temperature can shorten the operating potential window due to solvent decomposition [42].

The present study aims to assess the effect of operating temperature on the instantaneous heat generation rate and the associated electrochemical phenomena taking place in carbon-based EDLCs with either neat IL or diluted IL electrolytes cycled under a large potential window. The cells consisted of two activated carbon electrodes separated by a chemical resistant mesh immersed in either neat N-butyl-N-methylpyrrolidinium bis(trifluoromethane sulfonyl)imide ($Pyr_{14}TFSI$) or 1 M $Pyr_{14}TFSI$ in PC electrolytes. The instantaneous heat generation rate at each electrode was measured using a recently developed *operando* isothermal calorimeter [43] at temperatures ranging from 5 to 80 °C under galvanostatic cycling and a potential window $\Delta\psi_s = 2.5$ V. The results were analyzed in terms of reversible and irreversible heat generation rates to provide insight into the physicochemical processes occurring during operation under large potential windows and high temperatures. The result can also be used in the design of thermal management solutions for EDLCs.

2. Background

2.1. Neat and diluted $pyr_{14}tfsi$ ionic liquid-based electrolytes

Ionic liquid $Pyr_{14}TFSI$ and its mixtures with organic solvents have been used widely as electrolytes in EDLCs due to their exceptional thermal, electrochemical, and cycling stability [26,31,44–46]. In fact, the operating potential window of neat $Pyr_{14}TFSI$ can be as high as ~ 3.5 V in the temperature range of 20 to 60 °C [29] compared with ≤ 3 V for organic electrolytes (e.g., ACN) and ~ 1 V for aqueous electrolytes [47]. The maximum potential windows of $Pyr_{14}TFSI$ mixtures in PC or ACN were recommended to be up to 3.5 V at 20 °C [29]. In addition, $Pyr_{14}TFSI$-based electrolytes show larger power and/or energy densities and better capacitance retention compared to the widely used organic electrolyte tetraethylammonium tetrafluoroborate ($TEABF_4$) in PC or ACN [26,48]. Furthermore, leakage current was about three times smaller in activated carbon (AC)-based EDLCs with $Pyr_{14}TFSI$, neat or diluted in PC, than with $TEABF_4$ in PC [49]. Indeed, the ionic conductivity of neat $Pyr_{14}TFSI$ is as low as ~ 2.0 mS/cm at 20 °C [50,51]. However, it depends strongly on temperature and increases to ~ 7.0 mS/cm at 60 °C [45,52]. In addition, the ionic conductivity of 1 M $Pyr_{14}TFSI$ in PC increased to 10.3 mS/cm at 25 °C [26].

2.2. Experimental calorimetry

2.2.1. Calorimeter device

Few experimental studies have investigated heat generation in EDLCs [43,53,54]. Dandeville et al. [53] measured time-dependent temperature evolution in two-electrode cells under galvanostatic cycling in a custom-made isothermal calorimeter. The heat generation rate in the entire cell was calculated by deconvoluting the measured time-dependent cell temperature during cycling [53]. Moreover, the heat generation rate in an AC-based EDLC cell electrode was assumed to be equally divided between the two electrodes [53]. In addition, heat generation was decomposed into (i) irreversible heat generation due to Joule heating and (ii) reversible heat generation caused by EDL formation [53].

More recently, Munteshari et al. [43,54] developed an *operando* isothermal calorimeter with integrated thermoelectric heat flux sensors to measure the instantaneous irreversible and reversible heat generation rates at each electrode of an EDLC cell. The authors investigated EDLC cells consisting of two identical AC-based electrodes immersed in aqueous or organic liquid electrolytes under constant current cycling I with potential window ≤ 1.0 V and at constant temperature of 20 °C [43,54]. The irreversible heat generation rate at each electrode was found to be proportional to I^2 under constant current cycling. The total irreversible heat generation in the cell was in excellent agreement with Joule heating expressed as $\bar{\dot{Q}}_J = R_s I^2$ where R_s is the internal resistance of the device measured from IR drop and found to be independent of current I [43]. The reversible heat generation rate at the positive electrode was (i) exothermic during

charging due to ion adsorption and (ii) endothermic during discharging due to ion desorption, as predicted theoretically [55,56]. However, at the negative electrode, the reversible heat generation rate was first endothermic and then exothermic during charging [43]. This was attributed to the presence of negatively charged functional groups associated with carboxymethyl cellulose (CMC) binder forming at the negative electrode and responsible for the overscreening effect [54]. In fact, the hydroxyl (−OH) and carboxymethyl ($-CH_2COONa$) functional groups of the CMC binder dissociate in 1 M $LiPF_6$ in EC:DMC organic electrolyte forming negatively charged functional groups ($-O^-$) and ($-CH_2COO^-$) that electrostatically attracted cations (e.g., Li^+), creating overscreening of the electrode surface [54,57]. In order to charge-balance the inner Helmholtz layer in the electrolyte, an additional layer of anions (e.g., PF_6^-) was required [54,57]. Thus, the negative electrode containing such functional groups was first charged by desorption of these sub-layer anions (endothermic) followed by cation adsorption (exothermic) [54,58].

2.2.2. Effect of potential window

As previously discussed, the operating potential window is an essential parameter for improving the specific energy of EDLCs. However, the operating potential window may be limited by the electrochemical stability window (ESW) of the electrolyte at a given temperature. Leyva-Garcia et al. [40] investigated the effect of potential window on the electrochemical performance of porous activated carbon (AC) electrodes with (i) neat $Pyr_{14}TFSI$ or (ii) 1 M $Pyr_{14}TFSI$ in PC electrolytes at 20 °C. The authors observed a redox peak in the CV curves at the negative electrode in 1 M $Pyr_{14}TFSI$ in PC electrolyte whereas no redox peak was observed in neat $Pyr_{14}TFSI$. They attributed this redox peak to PC solvent decomposition at the negative electrode under large potential [40]. Indeed, under large potential windows, PC decomposes (i) at the cathode to produce propane and hydrogen gases due to PC reduction or (ii) at the anode to produce carbon dioxide, propylene oxide, and other byproducts due to PC oxidation [40,59,60].

Moreover, Borenstein et al. [41] reported that a significant amount of FSI^- anions intercalated in the positive electrode of an AC-based EDLC with neat $Pyr_{14}FSI$ ionic liquid electrolyte after 3000 galvanostatic cycles at $\Delta\psi_s = 3.4$ V [41]. This finding was confirmed by scanning electron microscopy and energy dispersive X-ray spectroscopy (SEM-EDX) measurements.

More recently, Munteshari et al. [61] studied the effects of potential window ranging from 1 to 4 V on the heat generation rate in cells consisting of two identical porous AC electrodes with either neat $Pyr_{14}TFSI$ or 1 M $Pyr_{14}TFSI$ in PC electrolytes using *operando* isothermal calorimeter at 20 °C. For devices with neat $Pyr_{14}TFSI$ electrolyte, an endothermic dip appeared in the instantaneous heat generation rate at the positive electrode for cell potential window of 4.0 V as a result of $TFSI^-$ intercalation, as confirmed by EDX spectroscopy [61]. On the other hand, for devices with 1 M $Pyr_{14}TFSI$ in PC electrolyte, an endothermic dip appeared in the instantaneous heat generation rate at the negative electrode starting from cell potential window of 3.0 V as a result of PC decomposition [61]. In addition, the irreversible and reversible heat generation rates at both electrodes increased with increasing potential window for given current in both neat and diluted $Pyr_{14}TFSI$ electrolytes [61]. For 1 M $Pyr_{14}TFSI$ in PC electrolyte, the irreversible heat generation rate increased sharply as the potential window increased from 3.0 V to 3.5 V due to PC decomposition at potential window of 3.5 V [61]. Furthermore, unlike previous studies [43,54] with cell potential window $\Delta\psi_s \leq 1$ V, the total irreversible heat generation rate of the entire cell exceeded Joule heating for $\Delta\psi_s > 1$ V in both neat and diluted $Pyr_{14}TFSI$ electrolytes [61]. This additional irreversible heat generation rate was attributed to the heat generation associated with charge redistribution in the porous carbon electrode and identified as the leakage current dissipated through the pore resistance [61].

2.2.3. Effect of temperature

Numerous studies have investigated the effect of temperature on the performance of EDLCs with various electrolytes [16,18,19,42,62–71]. Electrochemical measurement methods such as galvanostatic charge–discharge cycling (GCD), cyclic voltammetry (CV), and electrochemical impedance spectroscopy (EIS) were performed within the temperature range of −40 to 100 °C on (i) test cells in three-electrode setup [67] and two-electrode cells [19,62,64,71] and on (ii) commercial EDLC devices and module [16,42,62,63,65,66]. The specific capacitance was found to increase with increasing temperature as a result of increasing ion mobility [19,62,66,67,72]. For the same reason, the cell internal resistance R_s decreased with increasing temperature in organic [16,19,66] as well as in ILs [62,73] electrolytes. However, increasing the operating temperature can have a negative effect on the self-discharge rate of EDLCs [14,15,17]. In fact, at high temperatures, ions feature higher desorption rates leading to device self-discharge [16,71,74]. Moreover, high operating temperatures and/or high applied voltages can lead to accelerated aging of EDLCs due to thermal and electrochemical degradation of the electrolyte and/or of the electrode materials [18,42,75]. First, for temperatures larger than the onset of decomposition temperature, electrolytes may decompose to produce gases such as carbon monoxide (CO), hydrogen (H_2), and other organic byproducts, as previously discussed [75]. These gases can lead to pressure rise inside the cell leading potentially to explosions [76]. The gases generated can also block access to the pores in the electrodes to the liquid electrolyte, leading to an increase in cell resistance and a decrease in the device capacitance [42,75]. High temperatures can also accelerate decomposition reactions in the electrolyte and/or in the electrode by oxidation/reduction reactions producing solid byproducts [77]. These byproducts can attach onto the electrode/electrolyte interface thus reducing the electrode active surface area [77].

Most recently, we investigated the effect of operating temperature on irreversible and reversible heat generation rates in a full-cell device consisting of two identical porous AC electrodes with 1 M $Pyr_{14}TFSI$ in PC electrolyte cycled with a potential window of 1 V [73]. The instantaneous heat generation rate at each electrode was measured at temperatures ranging from 20 to 60 °C [73] using an *operando* isothermal calorimeter [43]. The measurement were similar at both electrodes and proportional to I^2. Their sum was equal to Joule heating given by $\bar{Q}_J(T) = R_s(T)I^2$ where $R_s(T)$ is the internal resistance of the device measured at temperature T and I is the imposed current. The internal resistance $R_s(T)$ and thus $\bar{Q}_J(T)$ decreased with increasing temperature due to the increasing electrolyte ionic conductivity [73]. However, the reversible heat generation rate was found to be independent of temperature for the potential window of 1 V considered [73].

Overall, previous calorimetric studies have investigated the instantaneous heat generation rate in EDLCs (i) with aqueous or organic electrolytes for potential window $\Delta\psi_s \leq 1.0$ V at 20 °C [43], (ii) with neat $Pyr_{14}TFSI$ or 1 M $Pyr_{14}TFSI$ in PC for potential window varying from 1.0 V to 4.0 V at 20 °C [61], and (iii) with 1 M $Pyr_{14}TFSI$ in PC for potential window of 1.0 V and temperature varying from 20 to 60 °C [73]. The present study aims to assess the effect of temperature on reversible and irreversible heat generation rates in EDLC with IL-based electrolyte under galvanostatic cycling. Here, a potential window of 2.5 V was chosen as a stable potential window for both neat $Pyr_{14}TFSI$ and 1 M $Pyr_{14}TFSI$ in PC electrolytes at 20 °C. The operating temperature was varied between 5 and 80 °C to assess its effect on the heat generation rate. The results can also be used to design thermal management strategies for EDLCs and to determine the operating limits of the devices.

3. Materials and methods

3.1. Electrode and device fabrication

Activated carbon slurries were prepared by mixing (i) activated carbon (YP-50F, Kuraray Chemical), (ii) TX-100 surfactant (DOW Chemical), (iii) carboxymethyl cellulose (CMC, DOW Chemical) used as a

thickening agent/binder, and (iv) styrene-butadiene rubber (SBR, MTI Corp.) as a binder, in DI water in an 80:5:1.5:13.5 weight ratio. The slurry was drop-casted onto carbon-coated aluminum current collector sheets (MTI Corp.) with 1×1 cm^2 footprint area. The current collectors were previously treated by oxygen plasma to enhance their hydrophilicity and ensure uniform spreading of the slurry. The mass loading on each electrode was 2.5 mg of slurry (2.0 mg of AC) corresponding to an electrode thickness of about 60 μm. Note that the conductive carbon coating on Al-foil (MTI Corp.) is very thin (1 μm) compared to the electrodes and the 16 μm thick Al foil. In addition, carbon is a good electrical and thermal conductor. Therefore, its effect on the heat transfer between the electrode and the heat flux sensors can be considered to be negligible. The electrodes were dried in a vacuum oven at 120 °C for 24 h before being assembled into full-cell devices in a glove box under argon (Ar) atmosphere (< 1 ppm H_2O/O_2).

The EDLC devices consisted of two identical activated carbon electrodes separated by a 1 mm-thick chemical-resistant polypropylene mesh serving as a separator and as thermal insulator. The devices were assembled using either (i) neat Pyr_{14}TFSI (Device 1) or (ii) 1 M Pyr_{14}TFSI diluted in PC electrolyte (Device 2). The concentration of 1 M Pyr_{14}TFSI in PC corresponds to the maximum ionic conductivity (~ 8.3 mS/cm) and the lowest viscosity (~ 5 mPa s) at 20 °C [78]. Finally, the device was assembled and placed in the calorimeter compartment inside a glove box under Ar atmosphere before being taken out for isothermal calorimetric measurements at temperatures ranging from 5 to 80 °C. The isothermal calorimeter was described in detail in Ref. [43].

3.2. Device characterization

First, linear sweep voltammetry (LSV) was employed to determine the electrochemical stability window (ESW) of the electrolytes with either (i) neat Pyr_{14}TFSI or (ii) 1 M Pyr_{14}TFSI in PC incorporated in a two-terminal stainless steel coin cell (MTI Corp). Each coin cell, consisted of two AC-based electrodes (previously described) with a diameter of 9.5 mm (3/8″) separated by a Whatman glass microfiber D (Sigma-Aldrich). The coin cells were pressed to a pressure of ~ 6 MPa inside of an argon-rich glovebox. LSV measurements were performed at slow sweep rate of 0.1 mV/s at temperatures 20 °C, 40 °C, and 80 °C.

Second, cyclic voltammetry (CV) measurements were performed on Devices 1 and 2 inside the isothermal calorimeter at scan rate ν ranging from 5 to 30 mV/s at temperatures ranging from 5 to 80 °C. The device's gravimetric integral capacitance $C_{int,m}$ (in F/g) was evaluated from the CV curves as a function of scan rate ν according to [79],

$$C_{int,m}(\nu) = \frac{1}{m(\psi_{s,max} - \psi_{s,min})} \oint \frac{I(\psi_s)}{2\nu} d\psi_s. \quad (2)$$

Here, m is the total mass loading of AC in both electrodes (m = 4.0 mg) while $I(\psi_s)$ is the current measured at cell potential ψ_s. A cell potential window between $\psi_{s,min}$ = 0 V and $\psi_{s,max}$ = 2.5 V was selected because it fell within the ESW of both electrolytes investigated at room temperature [61].

Third, galvanostatic cycling combined with calorimetric measurements were performed on the devices at constant current I ranging from 1 to 5 mA at temperatures between 5 and 80 °C. For a given temperature, fifteen consecutive cycles were performed for each value of current I to guarantee that oscillatory steady state had been reached. In addition, the gravimetric differential capacitance $C_{diff,m}$ (in F/g) was estimated according to [79],

$$C_{diff,m}(I) = \frac{I}{m|d\psi_s/dt|} \quad (3)$$

where $|d\psi_s/dt|$ was estimated at the end of the discharging or charging step for each cycle at constant current I.

Furthermore, the internal resistance R_s was calculated from the IR drop observed at the charging/discharging transitions under galvanostatic cycling according to [80–83],

$$R_s(I) = \frac{\psi_s(t_c^+) - \psi_s(t_c^-)}{2I} \quad (4)$$

where $\psi_s(t_c^+)$ and $\psi_s(t_c^-)$ denote the potentials across the cell at the end of the charging step and immediately after the beginning of the discharging step, respectively. The IR drop, $\psi_s(t_c^+) - \psi_s(t_c^-)$, was obtained by estimating the cell potential $\psi_s(t_c^-)$ 10 ms after the beginning of the discharging step (i.e., $t_c^+ - t_c^- = 10$ ms), as suggested for supercapacitors by Zhao et al. [81] and successfully used in our previous studies [43,54,73].

3.3. Isothermal calorimeter

The *operando* isothermal calorimeter consisted of two thermoelectric heat flux sensors (gSKIN-XP by greenTEG) connecting to a data acquisition system (DAQ) and a cylindrical container made of polytetrafluoroethylene (PTFE) or Teflon [43]. Each heat flux sensor was 0.5 mm thick with a 10×10 mm^2 surface area and a resolution of 10 μW/cm^2. It was in thermal contact with a cylindrical copper rod, 15.9 mm in diameter and 19.5 mm in length, embedded in the center of a PTFE disc and flush with its surfaces (see Figure S1). The copper rod was used to conduct the heat generated in the electrode through the heat flux sensor to the cold plate, maintained at constant temperature [43]. An EDLC device placed inside the calorimeter was connected to a potentiostat (VSP-300 by BioLogic) and electrochemical measurements (CV and GCD) were performed simultaneously with calorimetric measurements. Note that, for the EDLC devices considered, at very low currents (< 1 mA) and/or with very small electrode mass loadings, heat generation rate was too small to achieve an acceptable signal to noise ratio.

The instantaneous heat generation rate at each electrode in Devices 1 and 2 was measured under galvanostatic cycling at constant temperatures ranging from 5 to 80 °C. The instantaneous heat generation rate $\dot{Q}_i(t)$ (in mW) at electrode "i" was found by measuring the heat transfer rate $q_i''(t)$ through the thermoelectric heat flux sensor and in thermal contact with the current collector such that [43],

$$\dot{Q}_i(t) = q_i''(t)A_i = \frac{\Delta V_i(t)}{S_i}A_i \qquad \text{with } i = + \text{ or } - \quad (5)$$

where $\Delta V_i(t)$ refers to the instantaneous voltage difference measured within each thermoelectric heat flux sensor in thermal contact with electrode "i". Here, subscript "i" refers to either the positive "+ " or negative "−" electrode. In addition, S_i denotes the temperature-dependent sensitivity of the heat flux sensor provided by the manufacturer (in μV/(W/m^2)) and A_i refers to the footprint area of the electrode (in cm^2). Then, the instantaneous total heat generation rate in the entire device (denoted by subscript "T") can be written as $\dot{Q}_T(t) = \dot{Q}_+(t) + \dot{Q}_-(t)$.

Moreover, the instantaneous heat generation rate $\dot{Q}_i(t)$ in each electrode can be decomposed as the sum of the reversible $\dot{Q}_{rev,i}(t)$ and irreversible $\dot{Q}_{irr,i}(t)$ heat generation rates, i.e., $\dot{Q}_i(t) = \dot{Q}_{rev,i}(t) + \dot{Q}_{irr,i}(t)$ [43,54]. Furthermore, by definition, time-averaging of the reversible heat generation rate $\dot{Q}_{rev,i}(t)$ at electrode "i" over a complete charging–discharging cycle yields $\bar{\dot{Q}}_{rev,i} = 0$. Thus, the time-averaged heat generation rate of $\dot{Q}_i(t)$ over a charging–discharging cycle period t_{cd} is equal to the time-averaged irreversible heat generation rate $\bar{\dot{Q}}_{irr,i}$ at electrode "i", i.e. [43,54],

$$\bar{\dot{Q}}_{irr,i} = \frac{1}{t_{cd}} \int_{(n_c-1)t_{cd}}^{n_c t_{cd}} \dot{Q}_i(t)\, dt \qquad \text{with } i = + \text{ or } - . \quad (6)$$

Here, n_c refers to the cycle number chosen to be large enough for $\dot{Q}_i(t)$ to have reached oscillatory steady state.

Finally, in order to compare the reversible heat generation rate at each electrode, the instantaneous reversible heat generation rate

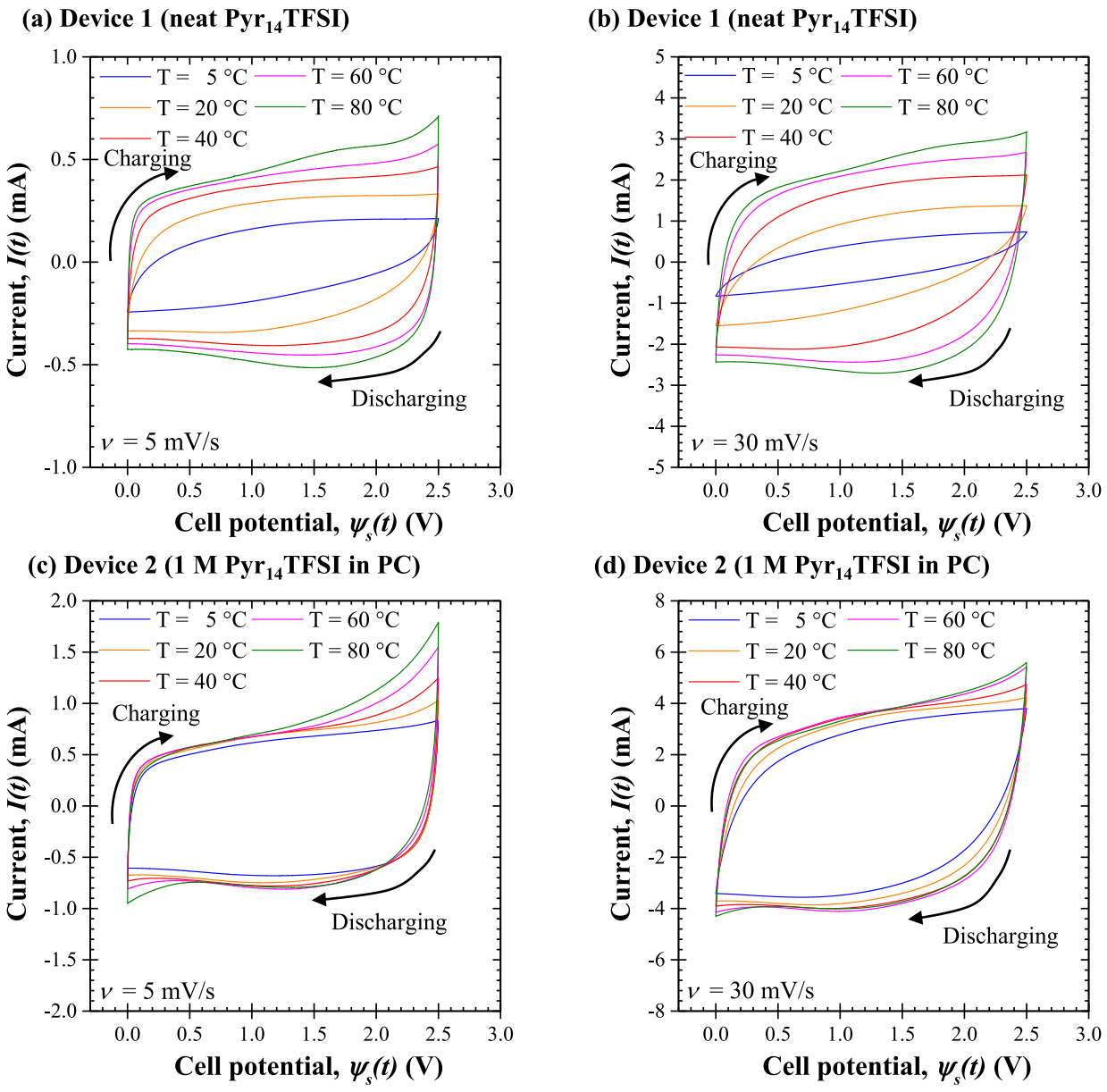

Fig. 1. Cyclic voltammograms of (a) Device 1 with neat $Pyr_{14}TFSI$ at ν = 5 mV/s and (b) at ν = 30 mV/s and (c) Device 2 with 1 M $Pyr_{14}TFSI$ in PC at ν = 5 mV/s and (d) at ν = 30 mV/s at temperature T ranging from 5 to 80 °C. The potential window ranged between $\psi_{s,min}$ = 0 V and $\psi_{s,max}$ = 2.5 V.

$\dot{Q}_{rev,i}(t)$ was time-averaged only over a charging period t_c according to [43,54],

$$\bar{\dot{Q}}^{c}_{rev,i} = \frac{1}{t_c}\int_{(n_c-1)t_{cd}}^{(n_c-1)t_{cd}+t_c} \dot{Q}_{rev,i}(t)\, dt \qquad \text{with } i = T,\ +,\ \text{or}\ -. \tag{7}$$

4. Results and discussion

4.1. Combined thermal and electrochemical stabilities

Figure S2 plots the linear sweep voltammograms (LSVs) for coin cells with the same AC electrodes as those used for calorimetric measurement with either neat $Pyr_{14}TFSI$ or 1 M $Pyr_{14}TFSI$ in PC electrolyte at scan rate of 0.1 mV/s and temperatures of 20 °C, 40 °C, and 80 °C. The current density $i(\psi_s)$ was defined as the ratio of the measured current response $I(\psi_s)$ during increasing coin cell potential ψ_s over the footprint area of the AC-based electrode in the coin cell, i.e., $i(\psi_s) = I(\psi_s)/A$ with $A = 0.7$ cm^2. The ESW depends on the choice of the cutoff current density beyond which the electrolyte is considered unstable. The cutoff current density typically ranges between 10 μA/cm^2 and 1 mA/cm^2 [84]. Figure S2 indicates that the ESW of the neat $Pyr_{14}TFSI$ electrolyte decreased with increasing temperature from above 5.5 V at 20 °C, to 4.6 V at 40 °C, and down to 3.7 V at 80 °C, based on the cutoff current density of 0.5 mA/cm^2 suggested in Refs [84–86].

Moreover, the ESW of the 1 M $Pyr_{14}TFSI$ in PC electrolyte was smaller than that of neat $Pyr_{14}TFSI$ for a given temperature due to the lower electrochemical stability of PC. In addition, the ESW decreased with increasing temperature from 4.2 V at 20 °C, to 3.7 V at 40 °C, and 3.3 V at 80 °C. Note that, partial decomposition of some electrolyte components may start below the reported ESW.

4.2. Cyclic voltammetry and gravimetric integral capacitance

Fig. 1(a) and (b) show the CV curves measured for Device 1 with neat $Pyr_{14}TFSI$ ionic liquid electrolyte at different temperatures between 5 and 80 °C for scan rate (a) ν = 5 mV/s and (b) ν = 30 mV/s, respectively. The CV curves at both scan rates featured leaf-like shape at low temperatures (≤ 20 °C) and became larger and more

rectangular with increasing temperature. These observations can be attributed to the increase in the ionic conductivity and to decreasing viscosity of neat IL with increasing temperature [45,52]. However, at T = 80 °C, small and broad peaks were observed around ψ_s ~ 1.0–2.0 V for both positive and negative sweeps. This may be attributed to reversible faradaic reactions involving electron transfer across the double layer, as observed in carbon-based SWNT at 100 °C [19] and graphene nanosheet at 60 °C in IL-based electrolytes [67]. Note also that similar peaks have been observed in EDLCs with AC electrodes and IL electrolytes and were attributed to traces amount of water in the electrolyte [87] or redox reactions between the electrolyte and functional groups on the carbon surface [87,88]. These broad current peaks were relatively small compared with the current from EDL formation and did not contribute significantly to the heat generation.

Similarly, Figs. 1(c) and 1(d) show the CV curves measured for Device 2 with 1 M $Pyr_{14}TFSI$ in PC electrolyte at different temperatures from 5 to 80 °C for scan rate (c) ν = 5 mV/s and (d) ν = 30 mV/s, respectively. Here, the CV curves were nearly rectangular at both low and high scan rates and did not change significantly with temperature, including at or below 20 °C. However, for slow charging at scan rate ν = 5 mV/s, all curves featured a peak at the end of the charging step near $\psi_{s,max}$ = 2.5 V that became more prominent as temperature increased. This was likely due to parasitic redox reactions associated with PC decomposition at higher potential and temperatures [89]. For faster charging at scan rate ν = 30 mV/s, this change in current response peak with temperature was small due to ion transport limitation within shorter charging time and/or slow redox reactions.

Furthermore, for a given scan rate ν and temperature T, Device 2 featured current $I(t)$ two to eight times larger than that in Device 1 owing to better ion mobility when $Pyr_{14}TFSI$ is dissolved in PC. Moreover, the area enclosed by the CV curves of Device 1 expanded significantly with increasing temperature. By contrast, those of Device 2 almost collapsed on top of each other except near $\psi_{s,min}$ and $\psi_{s,max}$. In other words, the increase in temperature contributed greatly to improving the performance of Device 1 while it had a modest effect on that of Device 2. This was due to the fact that neat $Pyr_{14}TFSI$ features ionic conductivity and viscosity that depend strongly on temperature [45,52], unlike $Pyr_{14}TFSI$ in PC.

Fig. 2(a) and (b) plot the gravimetric integral capacitance $C_{int,m}$ [Eq. (2)] as a function of scan rate ν for temperatures T ranging from 5 to 80 °C for Devices 1 and 2, respectively. The gravimetric integral capacitance $C_{int,m}$ of Devices 1 and 2 were, respectively, in the range of 5–25 F/g and 25–40 F/g corresponding to typical values for EDLC devices with similar electrode mass loading, electrolytes, and potential window [31,61,90–92]. Fig. 2 indicates that, for a given temperature, the gravimetric integral capacitance $C_{int,m}$ decreased with increasing scan rate ν, as typically observed in various EDLCs [43,93–95] and attributed to ion-diffusion limitation in porous electrodes at high scan rates [96]. In addition, the capacitance $C_{int,m}$ of Device 2 was about two to five times larger than that of Device 1 for any given scan rate ν and temperature T. This was likely due to the fact that the dielectric constant ϵ_r of PC was much larger than that of $Pyr_{14}TFSI$. For example, ϵ_r(PC) ≈ 65 [97,98] while ϵ_r($Pyr_{14}TFSI$) ≈ 11.7 to 14.7 at 25 °C [99–101]. Similarly, the viscosity of 1 M $Pyr_{14}TFSI$ in PC was much smaller than that of neat $Pyr_{14}TFSI$ leading to better wetting of the porous AC electrodes [67]. Moreover, Fig. 2(a) establishes that the capacitance of Device 1 increased significantly with increasing temperature from ~4 F/g at 5 °C to ~21 F/g at 80 °C due to the increasing ion mobility of the neat IL with increasing temperature. On the other hand, $C_{int,m}$ of Device 2 increased slightly from ~25 F/g at 5 °C to ~32 F/g at 60 °C. Interestingly, performance of Device 2 started degrading at 80 °C and high scan rates.

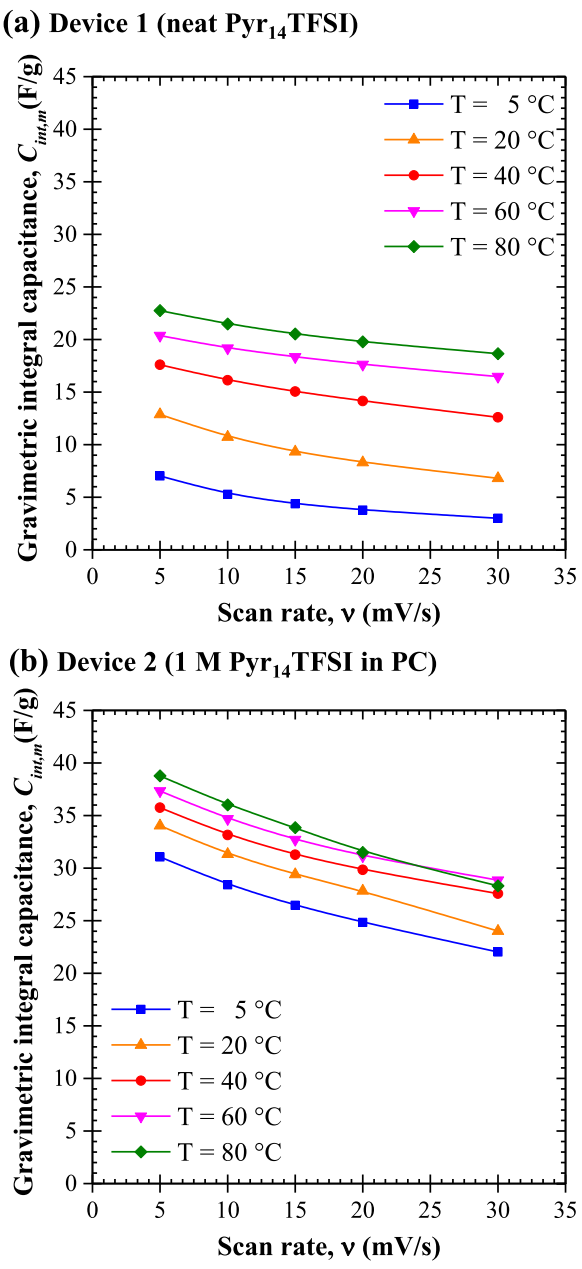

Fig. 2. Gravimetric integral capacitance $C_{int,m}$ [Eq. (2)] of (a) Device 1 with neat $Pyr_{14}TFSI$ and (b) Device 2 with 1 M $Pyr_{14}TFSI$ in PC electrolytes obtained from the CV curves shown in Fig. 1 for temperature T ranging from 5 to 80 °C and scan rate ν between 5 and 30 mV/s.

4.3. Galvanostatic cycling

Fig. 3 plots the internal resistance R_s obtained from the IR drop [Eq. (4)] observed in the galvanostatic charge–discharge curves (see Figure S3 in Supplementary Materials) as a function of temperature T ranging from 5 to 80 °C for (a) Device 1 and (b) Device 2 for imposed current I ranging from 1 to 5 mA. Note that, R_s did not depend significantly on the state-of-charge (SOC) for EDLCs. In fact, the internal resistances estimated from the IR drop either at the beginning or at the end of the charging step fell within 8% of each other for Device 1 and within 3% for Device 2 for all temperatures considered (see Figure S4 in Supplementary Materials). Fig. 3(a) establishes that the internal resistance R_s of Device 1 with neat $Pyr_{14}TFSI$ electrolyte (i) was independent of the imposed current I at any given temperature

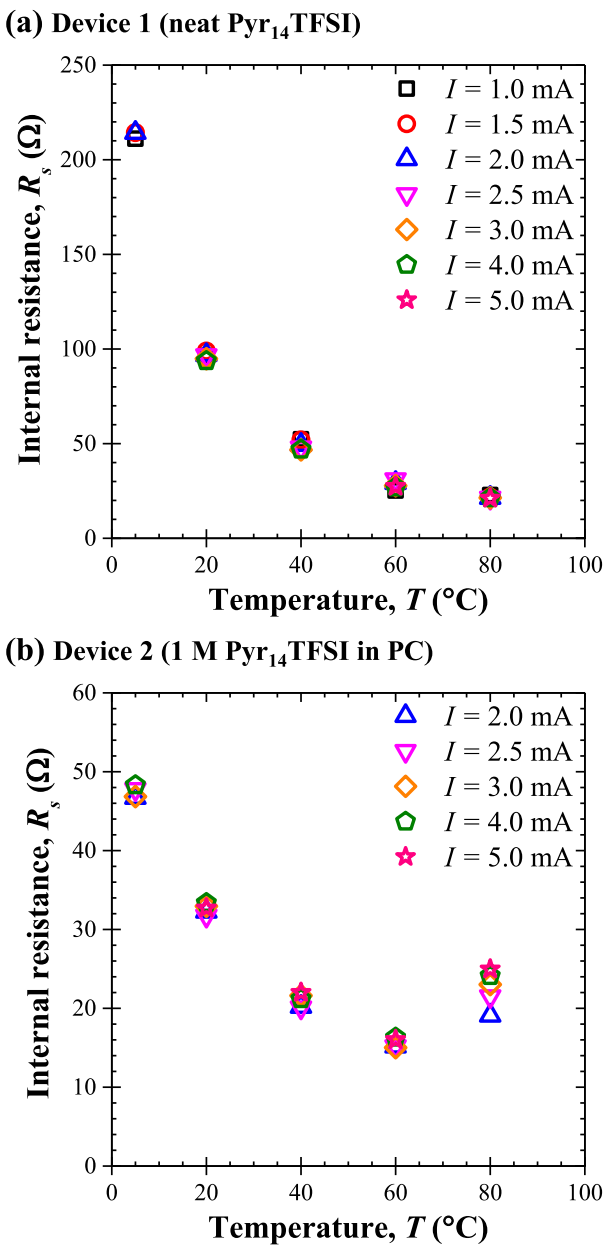

Fig. 3. Internal resistance R_s [Eq. (4)] as a function of temperature T ranging from 5 to 80 °C for (a) Device 1 with neat $Pyr_{14}TFSI$ and (b) Device 2 with 1 M $Pyr_{14}TFSI$ in PC for imposed current I ranging from 1 to 5 mA.

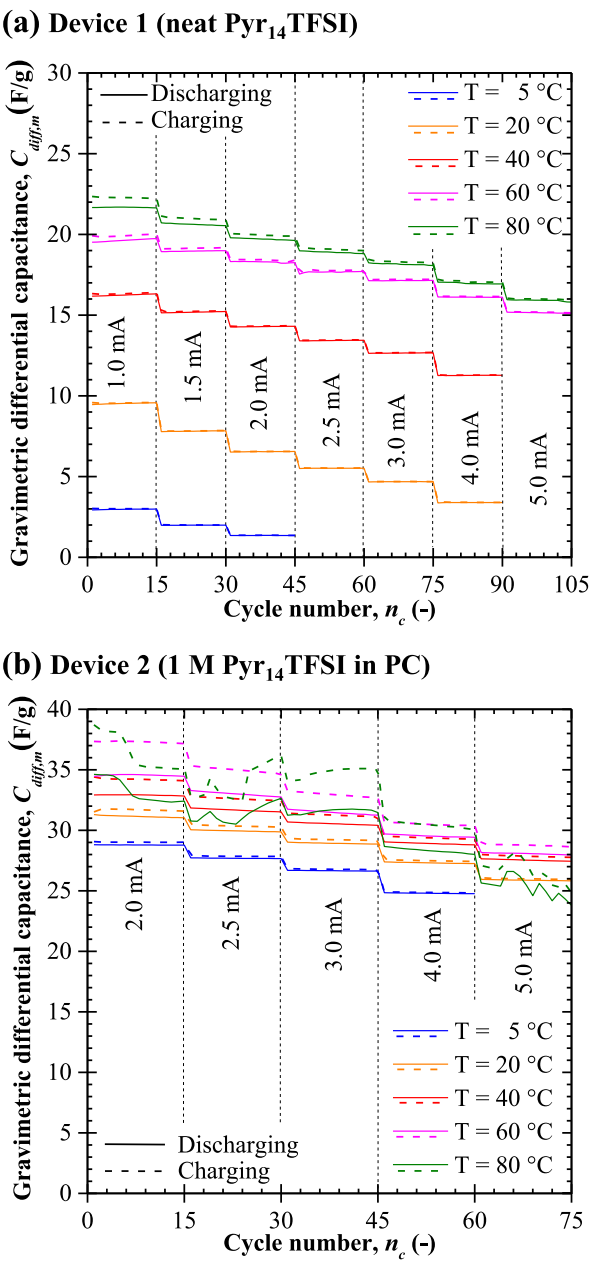

Fig. 4. Gravimetric differential capacitance $C_{diff,m}$ of (a) Device 1 with neat $Pyr_{14}TFSI$ and (b) Device 2 with 1 M $Pyr_{14}TFSI$ in PC as a function of cycle number n_c during charging and discharging steps at constant current I between 1 and 5 mA and at temperature T ranging from 5 to 80 °C.

and (ii) decreased significantly with increasing temperature from R_s = 213 ± 6 Ω at 5 °C to R_s = 22 ± 5 Ω at 80 °C. This observation was due mainly to the significant increase in ionic conductivity of neat $Pyr_{14}TFSI$ with temperature [45,52]. Similarly, Fig. 3(b) indicates that the internal resistance R_s of Device 2 with 1 M $Pyr_{14}TFSI$ in PC electrolyte was nearly independent of the imposed current I and decreased with increasing temperature T. In fact, the internal resistance R_s of Device 2 decreased from around R_s = 47 ± 3 Ω at 5 °C to R_s = 16 ± 5 Ω at 60 °C and was about two to four times smaller than that of Device 1 at any temperature up to 60 °C. Interestingly, the internal resistance R_s of Device 2 was larger at 80 °C than at 40 °C and 60 °C and depended on the imposed current I. This was due to PC decomposition at high temperatures and large potential windows. In fact, neat PC can lose about 10% of its initial mass within 4 h at 60 °C due to PC reduction at the negative electrode forming gaseous propane and/or hydrogen [59,102]. Note, however, that the rate of mass loss was smaller when mixed with ILs [59,102]. Regardless, PC degradation impeded access of the liquid electrolyte to the pores in the porous electrode resulting in large internal resistance [59,103]. Such increase in internal resistance with increasing temperature is responsible for thermal runaway [104].

Fig. 4 shows the gravimetric differential capacitance $C_{diff,m}$ calculated from galvanostatic charge–discharge cycles [Eq. (3)] as a function of cycle number n_c under different current I ranging from 1 to 5 mA for (a) Device 1 and (b) Device 2 at temperature T ranging between 5 and 80 °C. First, Fig. 4 indicates that $C_{diff,m}$ decreased with increasing current I in both devices. This could be due to ion diffusion limitation through the porous electrode under high current and fast charging. In addition, for any imposed current I in both devices, $C_{diff,m}$ increased with increasing temperature, except for Device 2 beyond T = 60 °C.

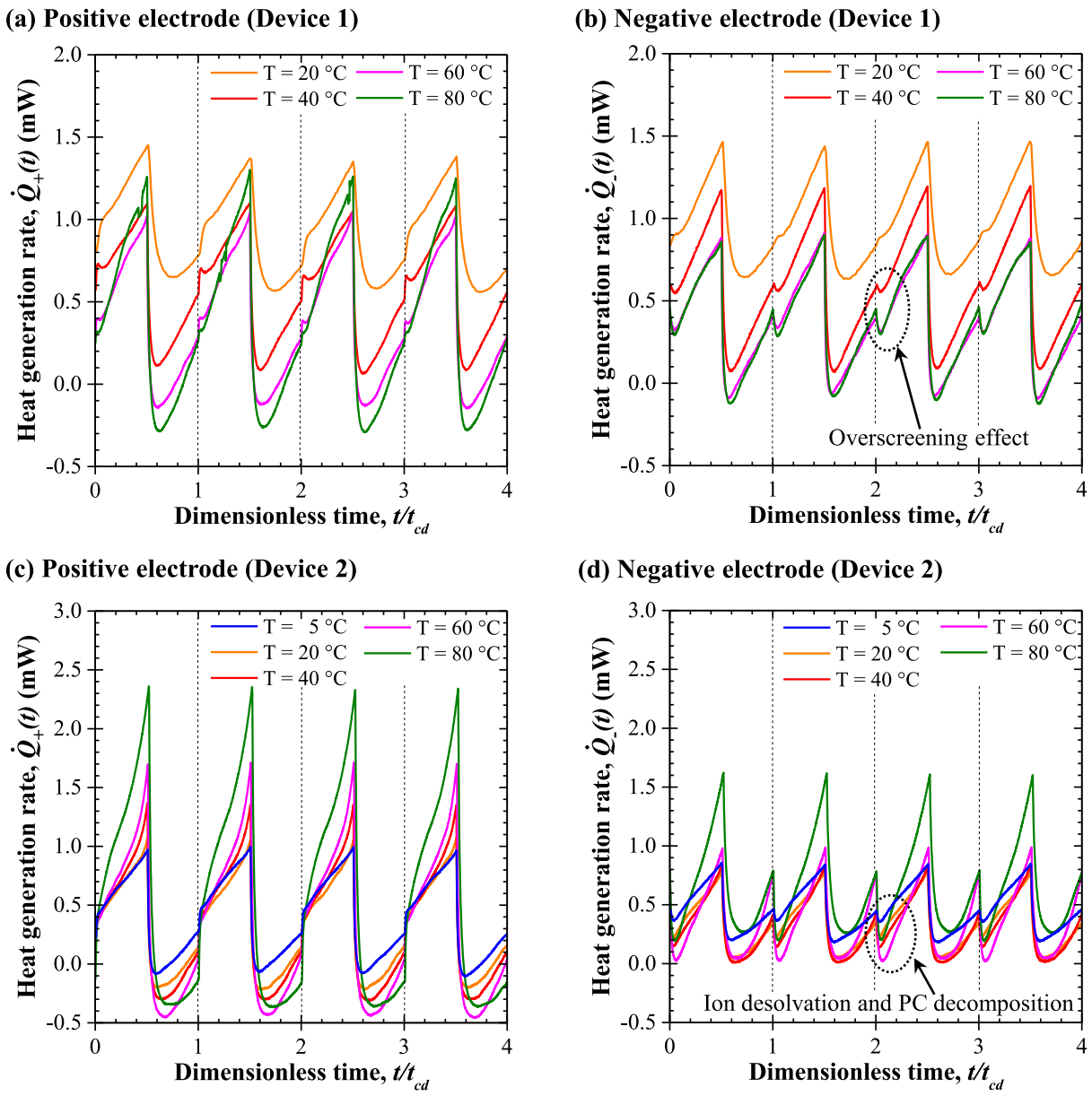

Fig. 5. Instantaneous heat generation rates as functions of dimensionless time t/t_{cd} for Device 1 with neat $Pyr_{14}TFSI$ electrolyte (a) $\dot{Q}_+(t)$ at the positive and (b) $\dot{Q}_-(t)$ at negative electrodes and for Device 2 with 1 M $Pyr_{14}TFSI$ in PC electrolyte (c) $\dot{Q}_+(t)$ at the positive and (d) $\dot{Q}_-(t)$ at negative electrodes for temperatures between 5 and 80 °C during four consecutive galvanostatic cycles under constant current I = 4 mA.

However, $C_{diff,m}$ of Device 1 was more sensitive to the temperature than that of Device 2. For example, in Device 1, $C_{diff,m}$ increased from 3.4 F/g at 20 °C to 16.1 F/g at 60 °C during discharging at I = 4 mA. By contrast, in Device 2, $C_{diff,m}$ increased only slightly from 27.4 F/g at 20 °C to 29.4 F/g at 60 °C also at I = 4 mA. Furthermore, $C_{diff,m}$ in both devices was slightly larger during charging than during discharging for any imposed current I and temperature T. This difference increased for smaller currents and higher temperatures. This could be attributed to self-discharge caused by (i) higher ion desorption rate at the electrode/electrolyte interface at high temperature and (ii) longer charging–discharging time t_{cd} at low current. Similar results were observed in devices composed of activated carbon electrodes with 1 M $TEABF_4$ or 1 M $EMIBF_4$ in ACN electrolytes [71]. Interestingly, $C_{diff,m}$ of Device 2 at T = 80 °C featured unusual fluctuations. This is consistent with the previous explanation that gaseous and/or solid byproducts generated during PC decomposition impeded electrolyte from entering porous electrodes.

4.4. Instantaneous heat generation rates

Fig. 5 shows the instantaneous heat generation rates (a) $\dot{Q}_+(t)$ at the positive electrode and (b) $\dot{Q}_-(t)$ at the negative electrode for Device 1 with neat $Pyr_{14}TFSI$ electrolyte as functions of dimensionless time t/t_{cd} for different temperatures ranging between 5 and 80 °C during four consecutive galvanostatic cycles under constant current I = 4 mA. Similarly, Fig. 5(c) and (d) show $\dot{Q}_+(t)$ and $\dot{Q}_-(t)$ for Device 2 with 1 M $Pyr_{14}TFSI$ in PC electrolyte, respectively. Note that, for Device 1, the imposed current I was limited to 2 mA at 5 °C due to an excessively large resistance and IR-drop and thus short charging–discharging time t_{cd} preventing sufficient data acquisition. For both devices, Fig. 5 indicates that the heat generation rate measurements were repeatable cycle after cycle for all temperatures considered. Note that the heat generation rate due to Joule heating – often considered as the only source of heat generation in EDLCs [9,15,17] – is constant over time under constant current cycling. Instead, experimental

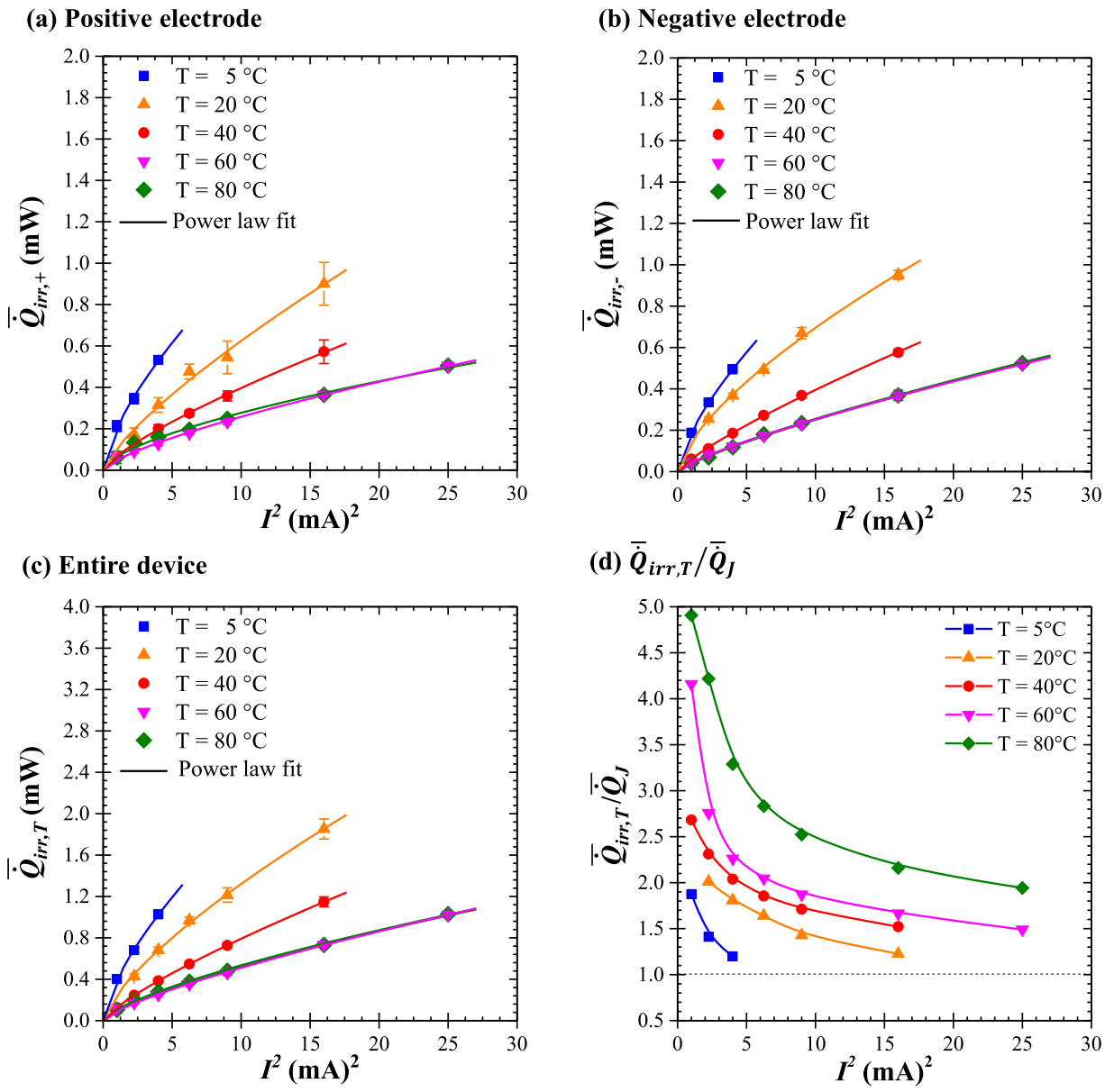

Fig. 6. Time-averaged irreversible heat generation rates (a) $\bar{\dot{Q}}_{irr,+}$ at the positive electrode, (b) $\bar{\dot{Q}}_{irr,-}$ at the negative electrode, (c) $\bar{\dot{Q}}_{irr,T}$ in the entire cell, and (d) $\bar{\dot{Q}}_{irr,T}/\bar{\dot{Q}}_J$ the ratio of total irreversible heat generation rate to Joule heating as functions of I^2 with imposed current I ranging from 1 to 5 mA for Device 1 with neat $Pyr_{14}TFSI$ electrolyte.

measurements in Fig. 5 featured strong temporal oscillations due to additional heat generation processes including reversible processes such as ion adsorption/desorption and solvation/desolvation.

Fig. 5(a) and (b) indicate that $\dot{Q}_+(t)$ and $\dot{Q}_-(t)$ at the positive and negative electrodes of Device 1 had similar magnitude for all temperatures, except for T = 80 °C when $\dot{Q}_+(t)$ was larger than $\dot{Q}_-(t)$. By contrast, in Device 2, the magnitude of $\dot{Q}_+(t)$ was consistently larger than that of $\dot{Q}_-(t)$ at any given temperature. This difference became larger with increasing temperature. Moreover, Fig. 5 indicates that $\dot{Q}_+(t)$ and $\dot{Q}_-(t)$ decreased with increasing temperature in Devices 1 and 2 for temperatures up to 60 °C. However, in both devices, the amplitude of the oscillations in $\dot{Q}_+(t)$ and $\dot{Q}_-(t)$ increased with increasing temperature. In Device 2 at 80 °C, both $\dot{Q}_+(t)$ and $\dot{Q}_-(t)$ increased due to the overall increase in internal resistance as a result of PC decomposition [Fig. 3(b)].

Furthermore, the instantaneous heat generation rate $\dot{Q}_+(t)$ at the positive electrode in both devices was strictly (i) exothermic during charging due to ion adsorption and (ii) endothermic during discharging due to ion desorption. This was consistent with results obtained from numerical simulations [55,56] and from previous experimental studies on AC-based EDLCs with aqueous, organic, or IL-based electrolytes [43,54,61,73]. On the other hand, the instantaneous heat generation rate $\dot{Q}_-(t)$ at the negative electrode of both Devices 1 and 2 featured an endothermic dip at the beginning of the charging step whose magnitude increased with increasing temperature. This dip was more significant in Device 2 than in Device 1. Indeed, for Device 1 with neat $Pyr_{14}TFSI$, a small endothermic dip can be observed at $T \geq 40$ °C for potential window of 2.5 V. A similar endothermic dip was also observed at T = 20 °C albeit for larger potential window of 3.5 V and 4 V in similar devices with neat $Pyr_{14}TFSI$ electrolyte [61]. This dip was attributed to the overscreening effect at the beginning of the charging step in presence of CMC binder at the negative AC-electrode with neat $Pyr_{14}TFSI$ electrolyte, as explained previously [54,61]. Similarly, the fact that the endothermic dip in $\dot{Q}_-(t)$ during charging was larger in Device 2 than in Device 1 could be due not only to the overscreening effect but also to the complete or partial endothermic desolvation of Pyr_{14}^+ cations of their PC solvation shell as they enter the AC nanopores to form an EDL [11,34,105,106].

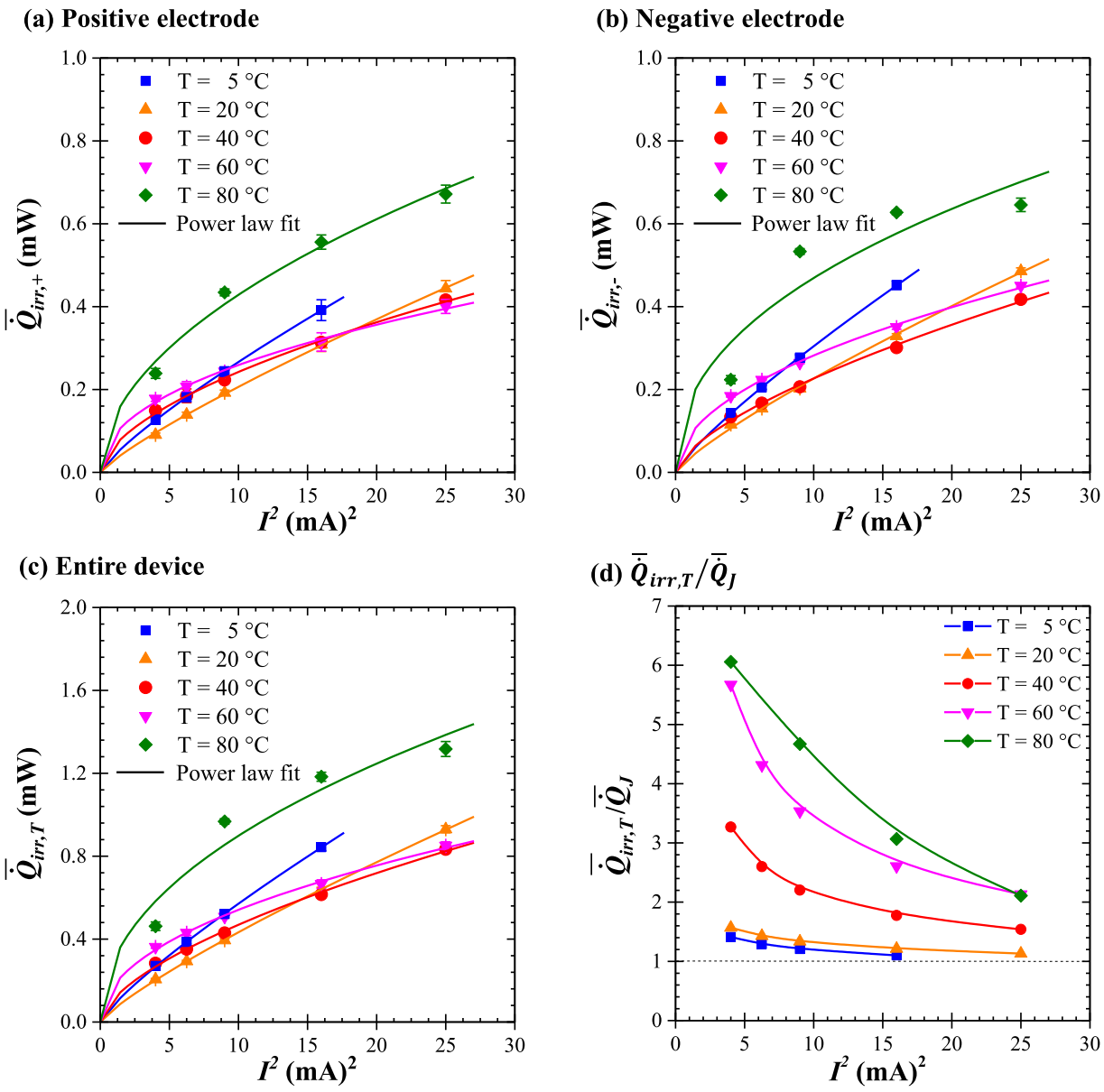

Fig. 7. Time-averaged irreversible heat generation rates (a) $\bar{\dot{Q}}_{irr,+}$ at the positive electrode, (b) $\bar{\dot{Q}}_{irr,-}$ at the negative electrode, (c) $\bar{\dot{Q}}_{irr,T}$ in the entire cell, and (d) $\bar{\dot{Q}}_{irr,T}/\bar{\dot{Q}}_J$ the ratio of total irreversible heat generation rate to Joule heating as functions of I^2 with imposed current I ranging from 1 to 5 mA for Device 2 with 1 M $Pyr_{14}TFSI$ in PC electrolyte.

Finally, the endothermic dip at the negative electrode of Device 2 became noticeably larger with increasing temperature as a result of increasing PC decomposition caused by endothermic PC reduction reaction [61]. Note that, this dip dominated at the beginning of the charging step due to the competing and sharply increasing exothermic heat generation rate associated with cation adsorption throughout the charging step [61].

4.5. Time-averaged irreversible heat generation rates

Figs. 6 and 7 plot the time-averaged irreversible heat generation rates (a) $\bar{\dot{Q}}_{irr,+}$ at the positive electrode, (b) $\bar{\dot{Q}}_{irr,-}$ at the negative electrode, (c) $\bar{\dot{Q}}_{irr,T}$ in the entire cell, and (d) the ratio $\bar{\dot{Q}}_{irr,T}/\bar{\dot{Q}}_J$ of total irreversible heat generation rate to Joule heating as functions of I^2 with imposed current I ranging from 1 to 5 mA and temperature T varying between 5 and 80 °C for Device 1 and Device 2, respectively. The error bars correspond to two standard deviation or 95% confidence interval estimated by evaluating $\bar{\dot{Q}}_{irr,i}$ over five consecutive galvanostatic cycles. In addition, Joule heating was estimated as

$$\bar{\dot{Q}}_J = \bar{R}_s(T)I^2 \tag{8}$$

where $\bar{R}_s(T)$ is the average internal resistance reported in Fig. 3, except for Device 2 at 80 °C when variations in $R_s(T)$ with imposed current I were accounted for.

Figs. 6 and 7 indicate that $\bar{\dot{Q}}_{irr,+}$ and $\bar{\dot{Q}}_{irr,-}$ were fairly similar in each device and for any given temperature. This was attributed to the fact that (i) the positive and negative electrodes were synthesized in the same manner and should be nearly identical and (ii) the diffusion coefficients of Pyr_{14}^+ cations and $TFSI^-$ anions were similar in each electrolyte considered [37,52,90,107]. In fact, the ratio of the diffusion coefficients of Pyr_{14}^+ to that of $TFSI^-$ in neat $Pyr_{14}TFSI$, i.e., D_+/D_- was reported to be equal to 1.2 at 20 °C and 1.1 at 40 °C [107] and approaching 1.0 as the temperature increases [37]. Similarly, in Device 2 (Fig. 7), $D_+ \approx D_-$ in 1 M of $Pyr_{14}TFSI$ dissolved in PC at 20 °C [52,90]. Therefore, the ionic conductivity of the electrolyte in each half cell were similar at all temperatures in each device. The slight differences between $\bar{\dot{Q}}_{irr,+}$ and $\bar{\dot{Q}}_{irr,-}$ could be due to differences in the

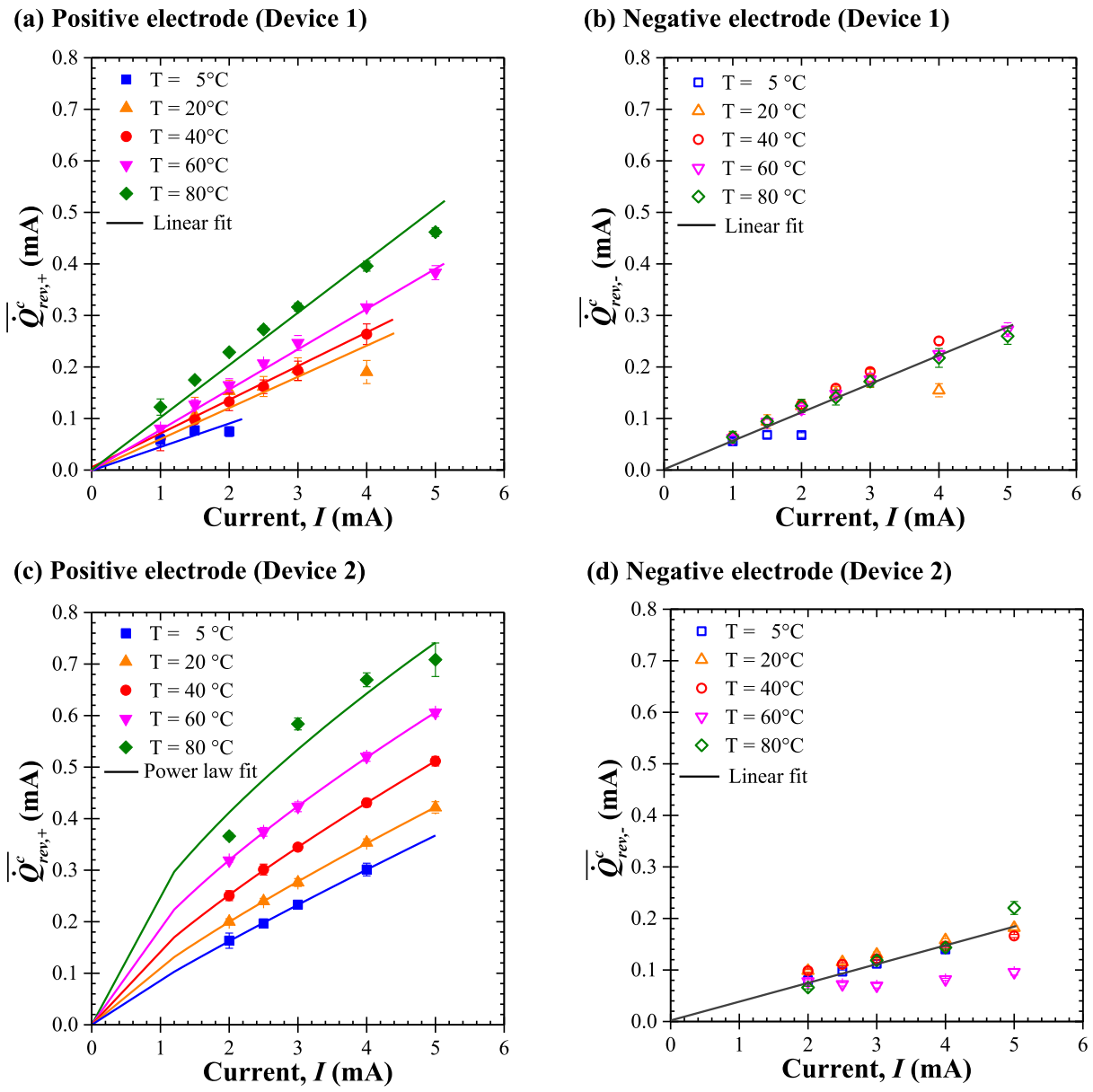

Fig. 8. Time-averaged reversible heat generation rates during the charging step as functions of imposed current I ranging between 1 and 5 mA for Device 1 with neat $Pyr_{14}TFSI$ electrolyte (a) $\bar{\dot{Q}}^{c}_{rev,+}$ at the positive and (b) $\bar{\dot{Q}}^{c}_{rev,-}$ at negative electrodes and for Device 2 with 1 M $Pyr_{14}TFSI$ in PC electrolyte (c) $\bar{\dot{Q}}^{c}_{rev,+}$ at the positive and (d) $\bar{\dot{Q}}^{c}_{rev,-}$ at negative electrodes for temperatures between 5 and 80 °C.

electrode mass loading. In addition, the irreversible heat generation rates $\bar{\dot{Q}}_{irr,+}$ and $\bar{\dot{Q}}_{irr,-}$ in Device 2 were typically smaller than those in Device 1 due, in part, to its smaller internal resistance R_s (Fig. 3).

Moreover, Fig. 6 establishes that the time-averaged irreversible heat generation rates $\bar{\dot{Q}}_{irr,+}$ and $\bar{\dot{Q}}_{irr,-}$ at the positive and negative half-cells as well as $\bar{\dot{Q}}_{irr,T}$ in the entire Device 1 decreased significantly with increasing temperature from 5 to 80 °C. This was due, in part, to the fact that the ionic conductivity of neat $Pyr_{14}TFSI$ and the wettability of the electrodes increased sharply with increasing temperature. By contrast, Fig. 7 establishes that $\bar{\dot{Q}}_{irr,+}$, $\bar{\dot{Q}}_{irr,-}$, and $\bar{\dot{Q}}_{irr,T}$ in Device 2 decreased slightly between 5 and 20 °C and were nearly independent of temperature between 20 to 60 °C for any given current. These observations are surprising given the decrease in internal resistance $\bar{R}_s(T)$ of Device 2 with increasing temperature from 5 to 60 °C [Fig. 3(b)]. It suggested that Joule heating was not the only source of irreversible heat generation. However, $\bar{\dot{Q}}_{irr,+}$, $\bar{\dot{Q}}_{irr,-}$, and $\bar{\dot{Q}}_{irr,T}$ increased significantly at 80 °C in Device 2 due to the partial PC decomposition resulting in electrode pore blockage [42,75] and increasing cell resistance [Fig. 3(b)].

Furthermore, $\bar{\dot{Q}}_{irr,+}$, $\bar{\dot{Q}}_{irr,-}$, and $\bar{\dot{Q}}_{irr,T}$ in EDLCs with aqueous and organic electrolytes at 20 °C [43,54] and in IL-based electrolyte between 20 to 60 °C [73] all for cell potential window $\Delta\psi_s \leq 1$ V were linearly proportional to I^2. In fact, the total heat generation rate $\bar{\dot{Q}}_{irr,T}$ was equal to Joule heating, i.e., $\bar{\dot{Q}}_J = R_s I^2$. By contrast, $\bar{\dot{Q}}_{irr,+}$, $\bar{\dot{Q}}_{irr,-}$, and $\bar{\dot{Q}}_{irr,T}$ in both Devices 1 and 2 with $\Delta\psi_s = 2.5$ V did not vary linearly with I^2, as indicated by power law fit. In fact, the total irreversible heat generation rate $\bar{\dot{Q}}_{irr,T}$ in both Devices 1 and 2 exceeded Joule heating $\bar{\dot{Q}}_J$ for any temperatures between 5 and 80 °C, i.e., $\bar{\dot{Q}}_{irr,T}/\bar{\dot{Q}}_J > 1$. The ratio $\bar{\dot{Q}}_{irr,T}/\bar{\dot{Q}}_J$ increased with increasing temperature and decreasing current in both Devices 1 and 2. Similar results were also observed in similar devices cycled at 20 °C under large potential windows $\Delta\psi_s$ up to 4 V [61]. This can be attributed to a combination of phenomena namely (i) the charge redistribution in porous electrodes caused by higher ions desorption rate with increasing temperature and modeled as the

leakage current flowing through the pore resistance [14,16,61,71,74], (ii) the longer charging–discharging time t_{cd} at low current (see Figure S5 in Supplementary Materials), and (iii) PC solvent decomposition increasing with increasing temperature in Device 2. In fact, the pore resistance is responsible for EDLC self-discharge and increased with increasing potential window [14,61,108,109].

4.6. Reversible heat generation rates

As previously discussed, the instantaneous irreversible heat generation rate $\dot{Q}_{irr,i}(t)$ cannot be solely attributed to Joule heating and may vary with time. Thus, the instantaneous reversible heat generation rate $\dot{Q}_{rev,i}(t) = \dot{Q}_i(t) - \dot{Q}_{irr,i}(t)$ cannot be estimated from our measurements. Instead, Fig. 8 shows the time-averaged reversible heat generation rates during a charging step [Eq. (7)] (a,c) $\bar{\dot{Q}}^c_{rev,+}$ at the positive electrode and (b,d) $\bar{\dot{Q}}^c_{rev,-}$ at the negative electrode as functions of current I for (a,b) Device 1 and (c,d) Device 2, respectively. Here also, the current I ranged from 1 to 5 mA and the temperature T from 5 to 80 °C and the error bars correspond to 95% confidence interval estimated by evaluating $\bar{\dot{Q}}^c_{rev,i}$ over five cycles. Fig. 8 indicates that, in both Devices 1 and 2, $\bar{\dot{Q}}^c_{rev,+}$ was systematically larger than $\bar{\dot{Q}}^c_{rev,-}$. This could be attributed to the fact that $TFSI^-$ anions are smaller (~ 0.7 nm) than Pyr^+_{14} cations (~ 1.1 nm). In fact, d'Entremont et al. [56] established theoretically that adsorption of smaller ions at a given electrode resulted not only in larger integral capacitance but also in larger reversible heat generation rate. Thus, $TFSI^-$ adsorption at the positive electrode during charging caused more reversible heat generation than Pyr^+_{14} adsorption at the negative electrode in Device 1 with neat $Pyr_{14}TFSI$. Similar arguments apply to Device 2 where solvated PC-Pyr^+_{14} ions were significantly larger than $TFSI^-$ ions in the 1 M $Pyr_{14}TFSI$ in PC electrolyte [56].

Moreover, for any given current and temperature, $\bar{\dot{Q}}^c_{rev,+}$ was typically larger in Device 2 than in Device 1 due to the fact that the capacitance of Device 2 was significantly larger than that of Device 1 (Figs. 2 and 4). By contrast, $\bar{\dot{Q}}^c_{rev,-}$ in Device 2 was smaller than in Device 1 as solvated PC-Pyr^+_{14} cations were larger compared to non-solvated Pyr^+_{14} cations in neat IL.

Fig. 8 also establishes that, for a given current in Devices 1 and 2, $\bar{\dot{Q}}^c_{rev,+}$ increased with increasing temperature whereas $\bar{\dot{Q}}^c_{rev,-}$ generally did not change significantly with temperature. This could be due to the endothermic dip previously observed in $\dot{Q}_-(t)$ at the negative electrode and associated with overscreening effect in Devices 1 and 2 and/or with ion desolvation, and/or PC decomposition in Device 2. Indeed, the magnitude of this endothermic dip also increased with increasing temperature and compensated the rise in reversible heat generation caused by increasing capacitance.

Furthermore, in Device 1 with neat $Pyr_{14}TFSI$ [Fig. 8(a) and (b)], both $\bar{\dot{Q}}^c_{rev,+}$ and $\bar{\dot{Q}}^c_{rev,-}$ increased linearly with imposed current I for all temperatures considered. This was consistent with results from numerical simulations of EDLCs [55]. Similar observations were also made in previous experimental studies for EDLC cells consisting of AC-electrodes with organic or aqueous electrolytes for potential window $\Delta\psi_s \leq 1$ V [43,54] and with neat or diluted $Pyr_{14}TFSI$ electrolyte for different potential windows between 1 V to 4 V at 20 °C [61]. Similarly, in Device 2 with 1 M $Pyr_{14}TFSI$ diluted in PC [Fig. 8(c) and (d)], $\bar{\dot{Q}}^c_{rev,+}$ and $\bar{\dot{Q}}^c_{rev,-}$ increased fairly linearly with imposed current I except for temperatures $T = 60$ and 80 °C. This was due to the fact that the endothermic dip in the instantaneous heat generation rate at the negative electrode [Fig. 5(d)] attributed to overscreening effect and/or desolvation of Pyr^+_{14} from PC solvent shell and PC decomposition became significant at 60 and 80 °C.

5. Conclusion

This study reported the irreversible and reversible heat generation rates in two sets of AC-based EDLC devices with either (i) neat $Pyr_{14}TFSI$ or (ii) 1 M $Pyr_{14}TFSI$ in PC electrolytes. The measurements were performed in an isothermal *operando* calorimeter under galvanostatic cycling with potential window of 2.5 V and temperatures ranging from 5 to 80 °C. The instantaneous heat generation rate at each electrode was measured under galvanostatic cycling at temperatures between 5 and 80 °C for a potential window of 2.5 V. First, the instantaneous heat generation rate was similar at each electrode in neat IL. By contrast, it was smaller at the negative electrode than at the positive electrode in devices with diluted IL in PC. Large oscillations in the instantaneous heat generation rate were observed due to reversible processes such as ion adsorption/desorption and ion solvation/desolvation. In addition, endothermic dips appeared and grew with increasing temperature above 60 °C at the negative electrode at the beginning of the charging step. They were attributed to (i) overscreening effects in both electrolytes as well as to (ii) desolvation of Pyr^+_{14} cations and (iii) partial decomposition of PC in diluted IL electrolyte. Moreover, the irreversible heat generation rate in both devices decreased with increasing temperature due to the significant increase in the electrolyte ionic conductivity, particularly for the device with neat $Pyr_{14}TFSI$ electrolyte. The irreversible heat generation rates in the device with 1 M $Pyr_{14}TFSI$ in PC increased sharply at 80 °C as a result of PC decomposition. In addition, the total irreversible heat generation rate in each device exceeded Joule heating. This was attributed to additional irreversible heat generation caused by charge redistribution in the porous electrode and increasing leakage current due to ion desorption with increasing temperature. Second, in both EDLC devices, the time-averaged reversible heat generation rate over the charging step increased with increasing temperature and was larger at the positive than at the negative electrode due to the better accessibility of smaller $TFSI^-$ anions into subnanoscale pores compared with larger Pyr^+_{14} cations. Furthermore, the time-averaged reversible heat generation rate during charging at both electrodes increased linearly with imposed current except in the device with IL diluted in PC above 60 °C.

CRediT authorship contribution statement

Ampol Likitchatchawankun: Conceptualization, Methodology, Investigation, Data curation, Visualization, Writing - original draft. **Ryan H. DeBlock:** Investigation, Resources. **Grace Whang:** Investigation, Resources. **Obaidallah Munteshari:** Investigation, Data curation. **Matevž Frajnkovič:** Data curation. **Bruce S. Dunn:** Conceptualization, Methodology, Supervision. **Laurent Pilon:** Conceptualization, Methodology, Supervision, Writing - review & editing, Project administration.

Declaration of competing interest

The authors declare that they have no known competing financial interests or personal relationships that could have appeared to influence the work reported in this paper.

Acknowledgment

This work was supported as part of the Center for Synthetic Control Across Length-scales for Advancing Rechargeables (SCALAR), an Energy Frontier Research Center funded by the U.S. Department of Energy, Office of Science, Basic Energy Sciences under Award # DE-SC0019381.

Appendix A. Supplementary data

Supplementary material related to this article can be found online at https://doi.org/10.1016/j.jpowsour.2020.229368.

References

[1] B.E. Conway, Electrochemical Supercapacitors: Scientific Fundamentals and Technological Applications, Kluwer Academic/Plenum Publishers, New York, NY, 1999.

[2] J.B. Goodenough, H.D. Abruna, M.V. Buchanan, Basic Research Needs for Electrical Energy Storage: Report of the Basic Energy Sciences Workshop for Electrical Energy Storage, Tech. Rep., U.S. Department of Energy, 2007, http://dx.doi.org/10.2172/935429.

[3] A. Burke, R & D considerations for the performance and application of electrochemical capacitors, Electrochim. Acta 53 (3) (2007) 1083–1091.

[4] M. Winter, R.J. Brodd, What are batteries, fuel cells, and supercapacitors?, Chem. Rev. 104 (10) (2004) 4245–4270.

[5] L. Maharjan, S. Inoue, H. Akagi, A transformerless energy storage system based on a cascade multilevel PWM converter with star configuration, IEEE Trans. Ind. Appl. 44 (5) (2008) 1621–1630.

[6] A. Burke, Ultracapacitors: why, how, and where is the technology, J. Power Sources 91 (1) (2000) 37–50.

[7] M.D. Stoller, S. Park, Y. Zhu, J. An, R.S. Ruoff, Graphene-based ultracapacitors, Nano Lett. 8 (10) (2008) 3498–3502.

[8] J.R. Miller, Electrochemical capacitor thermal management issues at high-rate cycling, Electrochim. Acta 52 (4) (2006) 1703–1708.

[9] P. Guillemet, Y. Scudeller, T. Brousse, Multi-level reduced-order thermal modeling of electrochemical capacitors, J. Power Sources 157 (1) (2006) 630–640.

[10] P. Simon, Y. Gogotsi, Materials for electrochemical capacitors, Nature Mater. 7 (11) (2008) 845–854.

[11] F. Béguin, V. Presser, A. Balducci, E. Frackowiak, Carbons and electrolytes for advanced supercapacitors, Adv. Mater. 26 (14) (2014) 2219–2251.

[12] L.L. Zhang, Y. Gu, X. Zhao, Advanced porous carbon electrodes for electrochemical capacitors, J. Mater. Chem. A 1 (33) (2013) 9395–9408.

[13] F. Stoeckli, T.A. Centeno, Optimization of the characterization of porous carbons for supercapacitors, J. Mater. Chem. A 1 (23) (2013) 6865–6873.

[14] J. Schiffer, D. Linzen, D.U. Sauer, Heat generation in double layer capacitors, J. Power Sources 160 (1) (2006) 765–772.

[15] H. Gualous, H. Louahlia-Gualous, R. Gallay, A. Miraoui, Supercapacitor thermal modeling and characterization in transient state for industrial applications, IEEE Trans. Ind. Appl. 45 (3) (2009) 1035–1044.

[16] R. Kötz, M. Hahn, R. Gallay, Temperature behavior and impedance fundamentals of supercapacitors, J. Power Sources 154 (2) (2006) 550–555.

[17] M. Al Sakka, H. Gualous, J. Van Mierlo, H. Culcu, Thermal modeling and heat management of supercapacitor modules for vehicle applications, J. Power Sources 194 (2) (2009) 581–587.

[18] O. Bohlen, J. Kowal, D.U. Sauer, Ageing behaviour of electrochemical double layer capacitors: Part I. experimental study and ageing model, J. Power Sources 172 (1) (2007) 468–475.

[19] C. Masarapu, H.F. Zeng, K.H. Hung, B. Wei, Effect of temperature on the capacitance of carbon nanotube supercapacitors, ACS Nano 3 (8) (2009) 2199–2206.

[20] M. Galiński, A. Lewandowski, I. Stepniak, Ionic liquids as electrolytes, Electrochim. Acta 51 (26) (2006) 5567–5580.

[21] V. Ruiz, T. Huynh, S.R. Sivakkumar, A.G. Pandolfo, Ionic liquid–solvent mixtures as supercapacitor electrolytes for extreme temperature operation, RSC Adv. 2 (13) (2012) 5591–5598.

[22] C. Chiappe, D. Pieraccini, Ionic liquids: solvent properties and organic reactivity, J. Phys. Org. Chem. 18 (4) (2005) 275–297.

[23] C. Maton, N. De Vos, C.V. Stevens, Ionic liquid thermal stabilities: decomposition mechanisms and analysis tools, Chem. Soc. Rev. 42 (13) (2013) 5963–5977.

[24] M. Salanne, in: B. Kirchne, E. Perlt (Eds.), Chapter 2: Ionic Liquids for Supercapacitor Applications, in: Ionic Liquids II, Springer International Publishing, Cham, Switzerland, 2018, pp. 29–53.

[25] R. Hagiwara, J.S. Lee, Ionic liquids for electrochemical devices, Electrochemistry 75 (1) (2007) 23–34.

[26] A. Krause, A. Balducci, High voltage electrochemical double layer capacitor containing mixtures of ionic liquids and organic carbonate as electrolytes, Electrochem. Commun. 13 (8) (2011) 814–817.

[27] S. Pohlmann, A. Balducci, A new conducting salt for high voltage propylene carbonate-based electrochemical double layer capacitors, Electrochim. Acta 110 (2013) 221–227.

[28] R. Lin, P.-L. Taberna, S. Fantini, V. Presser, C.R. Pérez, F. Malbosc, N.L. Rupesinghe, K.B.K. Teo, Y. Gogotsi, P. Simon, Capacitive energy storage from −50 to 100 °C using an ionic liquid electrolyte, J. Phys. Chem. Lett. 2 (19) (2011) 2396–2401.

[29] A. Balducci, Electrolytes for high voltage electrochemical double layer capacitors: A perspective article, J. Power Sources 326 (2016) 534–540.

[30] W. Xu, C.A. Angell, Solvent-free electrolytes with aqueous solution-like conductivities, Science 302 (5644) (2003) 422–425.

[31] S. Pohlmann, B. Lobato, T.A. Centeno, A. Balducci, The influence of pore size and surface area of activated carbons on the performance of ionic liquid based supercapacitors, Phys. Chem. Chem. Phys. 15 (40) (2013) 17287–17294.

[32] G. Xiong, A. Kundu, T.S. Fisher, Thermal Effects in Supercapacitors, Springer, 2015.

[33] A. Lewandowski, A. Olejniczak, M. Galinski, I. Stepniak, Performance of carbon–carbon supercapacitors based on organic, aqueous and ionic liquid electrolytes, J. Power Sources 195 (17) (2010) 5814–5819.

[34] M.V. Fedorov, A.A. Kornyshev, Ionic liquids at electrified interfaces, Chem. Rev. 114 (5) (2014) 2978–3036.

[35] A. Balducci, F. Soavi, M. Mastragostino, The use of ionic liquids as solvent-free green electrolytes for hybrid supercapacitors, Appl. Phys. A 82 (4) (2006) 627–632.

[36] C. Arbizzani, G. Gabrielli, M. Mastragostino, Thermal stability and flammability of electrolytes for lithium-ion batteries, J. Power Sources 196 (10) (2011) 4801–4805.

[37] J. Reiter, S. Jeremias, E. Paillard, M. Winter, S. Passerini, Fluorosulfonyl-(trifluoromethanesulfonyl)imide ionic liquids with enhanced asymmetry, Phys. Chem. Chem. Phys. 15 (7) (2013) 2565–2571.

[38] S. Jeremias, M. Kunze, S. Passerini, M. Schoonhoff, Polymerizable ionic liquid with state of the art transport properties, J. Phys. Chem. B 117 (36) (2013) 10596–10602.

[39] K. Hayamizu, Y. Aihara, H. Nakagawa, T. Nukuda, W.S. Price, Ionic conduction and ion diffusion in binary room-temperature ionic liquids composed of [emim][BF_4] and LiBF_4, J. Phys. Chem. B 108 (50) (2004) 19527–19532.

[40] S. Leyva-García, D. Lozano-Castelló, E. Morallón, T. Vogl, C. Schütter, S. Passerini, A. Balducci, D. Cazorla-Amorós, Electrochemical performance of a superporous activated carbon in ionic liquid-based electrolytes, J. Power Sources 336 (2016) 419–426.

[41] A. Borenstein, R. Attias, O. Hanna, S. Luski, R.B. Kaner, D. Aurbach, A surprising failure mechanism in symmetric supercapacitors at high voltages, ChemElectroChem 4 (10) (2017) 2660–2668.

[42] A. Hammar, P. Venet, R. Lallemand, G. Coquery, G. Rojat, Study of accelerated aging of supercapacitors for transport applications, IEEE Trans. Ind. Electron. 57 (12) (2010) 3972–3979.

[43] O. Munteshari, J. Lau, A. Krishnan, B. Dunn, L. Pilon, Isothermal calorimeter for measurements of time-dependent heat generation rate in individual supercapacitor electrodes, J. Power Sources 374 (2018) 257–268.

[44] C. Arbizzani, M. Biso, D. Cericola, M. Lazzari, F. Soavi, M. Mastragostino, Safe, high-energy supercapacitors based on solvent-free ionic liquid electrolytes, J. Power Sources 185 (2) (2008) 1575–1579.

[45] S. Pohlmann, T. Olyschläger, P. Goodrich, J.A. Vicente, J. Jacquemin, A. Balducci, Azepanium-based ionic liquids as green electrolytes for high voltage supercapacitors, J. Power Sources 273 (2015) 931–936.

[46] A. Balducci, W.A. Henderson, M. Mastragostino, S. Passerini, P. Simon, F. Soavi, Cycling stability of a hybrid activated carbon//poly (3-methylthiophene) supercapacitor with N-butyl-N-methylpyrrolidinium bis(trifluoromethanesulfonyl)imide ionic liquid as electrolyte, Electrochim. Acta 50 (11) (2005) 2233–2237.

[47] S. Zhang, S. Brahim, S. Maat, High-voltage operation of binder-free CNT supercapacitors using ionic liquid electrolytes, J. Mater. Res. 33 (9) (2018) 1179–1188.

[48] A. Brandt, A. Balducci, Theoretical and practical energy limitations of organic and ionic liquid-based electrolytes for high voltage electrochemical double layer capacitors, J. Power Sources 250 (2014) 343–351.

[49] F. Soavi, C. Arbizzani, M. Mastragostino, Leakage currents and self-discharge of ionic liquid-based supercapacitors, J. Appl. Electrochem. 44 (4) (2014) 491–496.

[50] P. Johansson, L.E. Fast, A. Matic, G.B. Appetecchi, S. Passerini, The conductivity of pyrrolidinium and sulfonylimide-based ionic liquids: A combined experimental and computational study, J. Power Sources 195 (7) (2010) 2074–2076.

[51] M. Nádherná, J. Reiter, J. Moškon, R. Dominko, Lithium bis(fluorosulfonyl)imide–PYR_{14}TFSI ionic liquid electrolyte compatible with graphite, J. Power Sources 196 (18) (2011) 7700–7706.

[52] A. Balducci, R. Dugas, P.-L. Taberna, P. Simon, D. Plee, M. Mastragostino, S. Passerini, High temperature carbon–carbon supercapacitor using ionic liquid as electrolyte, J. Power Sources 165 (2) (2007) 922–927.

[53] Y. Dandeville, P. Guillemet, Y. Scudeller, O. Crosnier, L. Athouel, T. Brousse, Measuring time-dependent heat profiles of aqueous electrochemical capacitors under cycling, Thermochim. Acta 526 (1–2) (2011) 1–8.

[54] O. Munteshari, J. Lau, D.S. Ashby, B. Dunn, L. Pilon, Effects of constituent materials on heat generation in individual EDLC electrodes, J. Electrochem. Soc. 165 (7) (2018) A1547–A1557.

[55] A.L. d'Entremont, L. Pilon, First-principles thermal modeling of electric double layer capacitors under constant-current cycling, J. Power Sources 246 (2014) 887–898.

[56] A.L. d'Entremont, L. Pilon, Thermal effects of asymmetric electrolytes in electric double layer capacitors, J. Power Sources 273 (2015) 196–209.

[57] M.Z. Bazant, B.D. Storey, A.A. Kornyshev, Double layer in ionic liquids: Overscreening versus crowding, Phys. Rev. Lett. 106 (4) (2011) 046102.

[58] M.D. Levi, N. Levy, S. Sigalov, G. Salitra, D. Aurbach, J. Maier, Electrochemical quartz crystal microbalance (EQCM) studies of ions and solvents insertion into highly porous activated carbons, J. Am. Chem. Soc. 132 (38) (2010) 13220–13222.

[59] A. Brandt, C. Ramirez-Castro, M. Anouti, A. Balducci, An investigation about the use of mixtures of sulfonium-based ionic liquids and propylene carbonate as electrolytes for supercapacitors, J. Mater. Chem. A 1 (40) (2013) 12669–12678.

[60] M. Hahn, A. Würsig, R. Gallay, P. Novák, R. Kötz, Gas evolution in activated carbon/propylene carbonate based double-layer capacitors, Electrochem. Commun. 7 (9) (2005) 925–930.

[61] O. Munteshari, A. Borenstein, R.H. DeBlock, J. Lau, G. Whang, Y. Zhou, A. Likitchatchawankun, R. Kaner, B. Dunn, L. Pilon, In operando calorimetric measurements for activated carbon electrodes in neat or diluted ionic liquid electrolytes under large potential windows, ChemSusChem 13 (2020) 1–15.

[62] S.I. Fletcher, F.B. Sillars, R.C. Carter, A.J. Cruden, M. Mirzaeian, N.E. Hudson, J.A. Parkinson, P.J. Hall, The effects of temperature on the performance of electrochemical double layer capacitors, J. Power Sources 195 (21) (2010) 7484–7488.

[63] H. Michel, Temperature and dynamics problems of ultracapacitors in stationary and mobile applications, J. Power Sources 154 (2) (2006) 556–560.

[64] M. Arulepp, L. Permann, J. Leis, A. Perkson, K. Rumma, A. Jänes, E. Lust, Influence of the solvent properties on the characteristics of a double layer capacitor, J. Power Sources 133 (2) (2004) 320–328.

[65] P. Kreczanik, P. Venet, A. Hijazi, G. Clerc, Study of supercapacitor aging and lifetime estimation according to voltage, temperature, and RMS current, IEEE Trans. Ind. Electron. 61 (9) (2014) 4895–4902.

[66] P. Liu, M. Verbrugge, S. Soukiazian, Influence of temperature and electrolyte on the performance of activated-carbon supercapacitors, J. Power Sources 156 (2) (2006) 712–718.

[67] W. Liu, X. Yan, J. Lang, Q. Xue, Effects of concentration and temperature of $EMIMBF_4$/acetonitrile electrolyte on the supercapacitive behavior of graphene nanosheets, J. Mater. Chem. 22 (18) (2012) 8853–8861.

[68] W. Li, K. Xu, L. An, F. Jiang, X. Zhou, J. Yang, Z. Chen, R. Zou, J. Hu, Effect of temperature on the performance of ultrafine MnO_2 nanobelt supercapacitors, J. Mater. Chem. A 2 (5) (2014) 1443–1447.

[69] J.-G. Wang, Y. Yang, Z.-H. Huang, F. Kang, Effect of temperature on the pseudocapacitive behavior of freestanding MnO_2@ carbon nanofibers composites electrodes in mild electrolyte, J. Power Sources 224 (2013) 86–92.

[70] C. Yuan, X. Zhang, Q. Wu, B. Gao, Effect of temperature on the hybrid supercapacitor based on NiO and activated carbon with alkaline polymer gel electrolyte, Solid State Ion. 177 (13) (2006) 1237–1242.

[71] S. Park, S.-W. Kang, K. Kim, Competition between ionic adsorption and desorption on electrochemical double layer capacitor electrodes in acetonitrile solutions at different currents and temperatures, J. Power Sources 372 (2017) 8–15.

[72] B. Xu, F. Wu, R. Chen, G. Cao, S. Chen, Y. Yang, Mesoporous activated carbon fiber as electrode material for high-performance electrochemical double layer capacitors with ionic liquid electrolyte, J. Power Sources 195 (7) (2010) 2118–2124.

[73] A. Likitchatchawankun, G. Whang, J. Lau, O. Munteshari, B. Dunn, L. Pilon, Effect of temperature on irreversible and reversible heat generation rates in ionic liquid-based electric double layer capacitors, Electrochim. Acta 338 (2020) 135802.

[74] M. Ayadi, A. Eddahech, O. Briat, J.-M. Vinassa, Voltage and temperature impacts on leakage current in calendar ageing of supercapacitors, in: Proceedings of the 4th International Conference on Power Engineering, Energy and Electrical Drives, IEEE, Istanbul, Turkey, 2013, pp. 1466–1470, May 13–17, 2013.

[75] T. Umemura, Y. Mizutani, T. Okamoto, T. Taguchi, K. Nakajima, K. Tanaka, Life expectancy and degradation behavior of electric double layer capacitor part I, in: Proceedings of the 7th International Conference on Properties and Applications of Dielectric Materials, Vol. 3, IEEE, Nagoya, Japan, 2003, pp. 944–948, Jun 1–5, 2003.

[76] M. Hahn, R. Kötz, R. Gallay, A. Siggel, Pressure evolution in propylene carbonate based electrochemical double layer capacitors, Electrochim. Acta 52 (4) (2006) 1709–1712.

[77] A.M. Bittner, M. Zhu, Y. Yang, H.F. Waibel, M. Konuma, U. Starke, C.J. Weber, Ageing of electrochemical double layer capacitors, J. Power Sources 203 (2012) 262–273.

[78] S. Pohlmann, T. Olyschläger, P. Goodrich, J.A. Vicente, J. Jacquemin, A. Balducci, Mixtures of azepanium based ionic liquids and propylene carbonate as high voltage electrolytes for supercapacitors, Electrochim. Acta 153 (2015) 426–432.

[79] H. Wang, L. Pilon, Reply to comments on "Intrinsic limitations of impedance measurements in determining electric double layer capacitances" by H. Wang and L. Pilon [Electrochimica Acta 63 (2012) 55], Electrochim. Acta 63 (2012) 55.

[80] A. Burke, M. Miller, Testing of electrochemical capacitors: Capacitance, resistance, energy density, and power capability, Electrochim. Acta 55 (25) (2010) 7538–7548.

[81] S. Zhao, F. Wu, L. Yang, L. Gao, A.F. Burke, A measurement method for determination of DC internal resistance of batteries and supercapacitors, Electrochem. Commun. 12 (2) (2010) 242–245.

[82] M.D. Stoller, R.S. Ruoff, Best practice methods for determining an electrode material's performance for ultracapacitors, Energy Environ. Sci. 3 (9) (2010) 1294–1301.

[83] B.-A. Mei, O. Munteshari, J. Lau, B. Dunn, L. Pilon, Physical interpretations of nyquist plots for EDLC electrodes and devices, J. Phys. Chem. C 122 (1) (2017) 194–206.

[84] K. Xu, S.P. Ding, T.R. Jow, Toward reliable values of electrochemical stability limits for electrolytes, J. Electrochem. Soc. 146 (11) (1999) 4172.

[85] M. Morita, M. Goto, Y. Matsuda, Ethylene carbonate-based organic electrolytes for electric double layer capacitors, J. Appl. Electrochem. 22 (10) (1992) 901–908.

[86] M. Ishikawa, M. Ihara, M. Morita, Y. Matsuda, Electric double layer capacitors with new gel electrolytes, Electrochim. Acta 40 (13–14) (1995) 2217–2222.

[87] R. Yan, T. Heil, V. Presser, R. Walczak, M. Antonietti, M. Oschatz, Ordered mesoporous carbons with high micropore content and tunable structure prepared by combined hard and salt templating as electrode materials in electric double-layer capacitors, Adv. Sustain. Syst. 2 (2) (2018) 1–12.

[88] G.A. Tiruye, D. Muñoz-Torrero, T. Berthold, J. Palma, M. Antonietti, N. Fechler, R. Marcilla, Functional porous carbon nanospheres from sustainable precursors for high performance supercapacitors, J. Mater. Chem. A 5 (31) (2017) 16263–16272.

[89] Y. Cheng, H. Zhang, S. Lu, C.V. Varanasi, J. Liu, Flexible asymmetric supercapacitors with high energy and high power density in aqueous electrolytes, Nanoscale 5 (3) (2013) 1067–1073.

[90] S. Pohlmann, R.-S. Kühnel, T.A. Centeno, A. Balducci, The influence of anion–cation combinations on the physicochemical properties of advanced electrolytes for supercapacitors and the capacitance of activated carbons, ChemElectroChem 1 (8) (2014) 1301–1311.

[91] G. Moreno-Fernández, C. Schütter, J.M. Rojo, S. Passerini, A. Balducci, T.A. Centeno, On the interaction of carbon electrodes and non conventional electrolytes in high-voltage electrochemical capacitors, J. Solid State Electrochem. 22 (3) (2018) 717–725.

[92] X. Zhang, R.-S. Kühnel, S. Passerini, A. Balducci, Double-salt electrolytes for high voltage electrochemical double-layer capacitors, J. Solut. Chem. 44 (3–4) (2015) 528–537.

[93] C. Kim, Electrochemical characterization of electrospun activated carbon nanofibres as an electrode in supercapacitors, J. Power Sources 142 (1–2) (2005) 382–388.

[94] Y. Gao, Y.S. Zhou, M. Qian, X.N. He, J. Redepenning, P. Goodman, H.M. Li, L. Jiang, Y.F. Lu, Chemical activation of carbon nano-onions for high-rate supercapacitor electrodes, Carbon 51 (2013) 52–58.

[95] S.R.C. Vivekchand, C.S. Rout, K.S. Subrahmanyam, A. Govindaraj, C.N.R. Rao, Graphene-based electrochemical supercapacitors, J. Chem. Sci. 120 (1) (2008) 9–13.

[96] H. Wang, L. Pilon, Physical interpretation of cyclic voltammetry for measuring electric double layer capacitances, Electrochim. Acta 64 (2012) 130–139.

[97] R. Payne, I.E. Theodorou, Dielectric properties and relaxation in ethylene carbonate and propylene carbonate, J. Phys. Chem. 76 (20) (1972) 2892–2900.

[98] J. Barthel, R. Neueder, H. Roch, Density, relative permittivity, and viscosity of propylene carbonate + dimethoxyethane mixtures from 25 °C to 125 °C, J. Chem. Eng. Data 45 (6) (2000) 1007–1011.

[99] I. Krossing, J.M. Slattery, C. Daguenet, P.J. Dyson, A. Oleinikova, H. Weingärtner, Why are ionic liquids liquid? A simple explanation based on lattice and solvation energies, J. Am. Chem. Soc. 128 (41) (2006) 13427–13434.

[100] H. Weingärtner, P. Sasisanker, C. Daguenet, P.J. Dyson, I. Krossing, J.M. Slattery, T. Schubert, The dielectric response of room-temperature ionic liquids: effect of cation variation, J. Phys. Chem. B 111 (18) (2007) 4775–4780.

[101] M.-M. Huang, Y. Jiang, P. Sasisanker, G.W. Driver, H. Weingaärtner, Static relative dielectric permittivities of ionic liquids at 25 °C, J. Chem. Eng. Data 56 (4) (2011) 1494–1499.

[102] A.B. McEwen, S.F. McDevitt, V.R. Koch, Nonaqueous electrolytes for electrochemical capacitors: imidazolium cations and inorganic fluorides with organic carbonates, J. Electrochem. Soc. 144 (4) (1997) L84.

[103] K. Xu, Nonaqueous liquid electrolytes for lithium-based rechargeable batteries, Chem. Rev. 104 (10) (2004) 4303–4418.

[104] Q. Wang, P. Ping, X. Zhao, G. Chu, J. Sun, C. Chen, Thermal runaway caused fire and explosion of lithium ion battery, J. Power Sources 208 (2012) 210–224.

[105] J. Chmiola, C. Largeot, P.-L. Taberna, P. Simon, Y. Gogotsi, Desolvation of ions in subnanometer pores and its effect on capacitance and double-layer theory, Angew. Chem., Int. Ed. 47 (18) (2008) 3392–3395.

[106] X. Baokou, M. Anouti, Physical properties of a new deep eutectic solvent based on a sulfonium ionic liquid as a suitable electrolyte for electric double-layer capacitors, J. Phys. Chem. C 119 (2) (2015) 970–979.

[107] M. Kunze, S. Jeong, G.B. Appetecchi, M. Schönhoff, M. Winter, S. Passerini, Mixtures of ionic liquids for low temperature electrolytes, Electrochim. Acta 82 (2012) 69–74.

[108] J. Black, H.A. Andreas, Effects of charge redistribution on self-discharge of electrochemical capacitors, Electrochim. Acta 54 (13) (2009) 3568–3574.

[109] G. Madabattula, S. Kumar, Insights into charge-redistribution in double layer capacitors, J. Electrochem. Soc. 165 (3) (2018) A636–A649.